The `THOR` + `HELIOS` general circulation model: multiwavelength radiative transfer with accurate scattering by clouds/hazes

Russell Deitrick [1]★ Kevin Heng,[1,2] Urs Schroffenegger,[1] Daniel Kitzmann [1], Simon L. Grimm,[1] Matej Malik,[3] João M. Mendonça [4] and Brett M. Morris[1,5]

[1]*Center for Space and Habitability, University of Bern, Gesellschaftsstrasse 6, CH-3012 Bern, Switzerland*
[2]*Department of Physics, Astronomy and Astrophysics Group, University of Warwick, Coventry CV4 7AL, UK*
[3]*Department of Astronomy, University of Maryland, 4296 Stadium Drive, College Park, MD 20742, USA*
[4]*Technical University of Denmark, National Space Institute, Astrophysics and Atmospheric Physics, Elektrovej, DK-2800 Kgs. Lyngby, Denmark*
[5]*Physics Institute, Division of Space Research & Planetary Sciences, University of Bern, Sidlerstrasse 5, CH-3012 Bern, Switzerland*

ABSTRACT

General circulation models (GCMs) provide context for interpreting multiwavelength, multiphase data of the atmospheres of tidally locked exoplanets. In the current study, the non-hydrostatic `THOR` GCM is coupled with the `HELIOS` radiative transfer solver for the first time, supported by an equilibrium chemistry solver (`FastChem`), opacity calculator (`HELIOS-K`), and Mie scattering code (`LX-MIE`). To accurately treat the scattering of radiation by medium-sized to large aerosols/condensates, improved two-stream radiative transfer is implemented within a GCM for the first time. Multiple scattering is implemented using a Thomas algorithm formulation of the two-stream flux solutions, which decreases the computational time by about 2 orders of magnitude compared to the iterative method used in past versions of `HELIOS`. As a case study, we present four GCMs of the hot Jupiter WASP-43b, where we compare the temperature, velocity, entropy, and streamfunction, as well as the synthetic spectra and phase curves, of runs using regular versus improved two-stream radiative transfer and isothermal versus non-isothermal layers. While the global climate is qualitatively robust, the synthetic spectra and phase curves are sensitive to these details. A `THOR` + `HELIOS` WASP-43b GCM (horizontal resolution of about 4 deg on the sphere and with 40 radial points) with multiwavelength radiative transfer (30 k-table bins) running for 3000 Earth days (864 000 time-steps) takes about 19–26 d to complete depending on the type of GPU.

Key words: planets and satellites: atmospheres.

1 INTRODUCTION

1.1 Providing context for interpreting multiwavelength, multiphase data

Hot Jupiters are tidally locked, highly irradiated, hydrogen-dominated exoplanets (Burrows et al. 2010; Fortney et al. 2010). They are, of course, also 3D objects. Thus, to fully understand their atmospheres requires the procurement of emission and transmission spectra at different orbital phases or phase curves at different wavelengths (see Showman, Cho & Menou 2010; Burrows 2014b; Heng & Showman 2015; Parmentier, Showman & de Wit 2015; Showman, Tan & Parmentier 2020; Zhang 2020; for reviews), as well as constraints on their variability (e.g. Agol et al. 2010). With the *Hubble Space Telescope* (*HST*), measuring multiwavelength phase curves is restricted to hot Jupiters on short (<1 d) orbits. To date, these include WASP-43b (Stevenson et al. 2014), WASP-103b (Kreidberg et al. 2018), and WASP-18b (Arcangeli et al. 2019). With the upcoming *James Webb Space Telescope* (*JWST*), the procurement

of multiwavelength phase curves – and even eclipse maps (De Wit et al. 2012; Majeau, Agol & Cowan 2012) – of hot Jupiters is expected to become routine.

There is a rich body of literature on using 1D radiative-convective models to interpret the spectra of hot Jupiters (e.g. Seager & Sasselov 1998, 2000; Sudarsky, Burrows & Pinto 2000; Barman, Hauschildt & Allard 2001, 2005; Burrows, Sudarsky & Hubbard 2003; Sudarsky, Burrows & Hubeny 2003; Fortney et al. 2005, 2008; Burrows et al. 2007a, b; Tinetti et al. 2007; Burrows, Budaj & Hubeny 2008a; Burrows, Ibgui & Hubeny 2008b; Spiegel & Burrows 2010); see Burrows (2014a) for a review. Without resorting to parametrizations of the 3D dynamical and thermal structure, it is unclear how to self-consistently compute the day-side emission spectrum, nightside emission spectrum, transmission spectrum (associated with the terminator regions), multiwavelength phase curves and temporal variability of a tidally locked exoplanet. Some promising 2D or pseudo 2D approaches have been implemented (Tremblin et al. 2017; Gandhi & Jermyn 2020), but these generally still require 3D models for tuning and/or validation. To this end, general circulation models (GCMs) are an essential tool for understanding the relationship between atmospheric dynamics, radiation, chemistry, and the observational signatures of tidally locked exoplanets. GCMs also

★ E-mail: russell.deitrick@unibe.ch

provide context for atmospheric retrieval techniques that use 1D radiative transfer models (e.g. see Madhusudhan 2018; Barstow & Heng 2020 for reviews). Further, 3D information from GCMs is now being utilized directly in atmospheric retrievals (Flowers et al. 2019; Beltz et al. 2021; Wardenier et al. 2021).

1.2 Moving beyond Solar system-centric general circulation models

GCMs were originally developed for the study of the climate of Earth (e.g. Washington & Parkinson 2005). There is a long and enduring legacy of Earth GCMs (e.g. Adcroft et al. 2004; Anderson et al. 2004; Frierson, Held & Zurita-Gotor 2006, 2007; O'Gorman & Schneider 2008) and the study of the terrestrial climate as a heat engine (Peixóto & Oort 1984). The need to benchmark dynamical cores (the code that solves the fluid equations) was recognized by Held & Suarez (1994). Model hierarchies were proposed by Held (2005) as an approach for attaining deeper understanding of the ingredients of GCMs and how they interact.

For Jupiter, GCMs were developed as part of a debate on whether the Jovian jet/wind structures are shallow (e.g. Cho & Polvani 1996) or deep (e.g. Kaspi, Flierl & Showman 2009; Schneider & Liu 2009); see Vasavada & Showman (2005) for a review. This debate was settled recently for Jupiter (Kaspi et al. 2018) and also for Neptune and Uranus (Kaspi et al. 2013). A lesson learned from Jupiter GCMs is that the primitive equations of meteorology (see Appendix A for a review) are suitable for hot Jupiters, as long as the model domain is relatively small compared to the radius (Mayne et al. 2014b, 2017; Deitrick et al. 2020). Other lessons are difficult to generalize as Jupiter is a fast rotator (with a Rossby number well below unity), whereas tidally locked hot Jupiters are slow rotators (with Rossby numbers of the order of unity), implying that their jet/wind structures are qualitatively distinct (Menou et al. 2003). Furthermore, the energy budgets of hot Jovian atmospheres are dominated by stellar irradiation, rather than heating from the deep interior, implying that convection is suppressed and equator-to-pole circulation is present (Heng et al. 2011b). The high ($\gtrsim$1000 K) temperatures of hot Jovian atmospheres imply that the dominant opacity sources will be different from their Solar system counterpart.

The study of the atmospheric dynamics of hot Jupiters was pioneered by Showman & Guillot (2002) and Guillot & Showman (2002). The early works of Cho et al. (2003, 2008), Menou et al. (2003), and Menou & Rauscher (2009) treated only a shallow layer of hot Jovian atmospheres. Cooper & Showman (2005), Showman et al. (2008, 2009), and Rauscher & Menou (2010) were the first to use GCMs to model the deep atmospheres of hot Jupiters. Showman et al. (2009) was the first study to build multiwavelength radiative transfer into a hot Jupiter GCM, an effort that was followed up by Amundsen et al. (2016). Lewis et al. (2010) and Kataria et al. (2013) used GCMs to study irradiated exoplanets on highly eccentric orbits, building on the work of Langton & Laughlin (2008). Heng et al. (2011a) generalized the GCM benchmark tests of Held & Suarez (1994) for tidally locked exoplanets, based on the work of Menou & Rauscher (2009), Merlis & Schneider (2010), and Rauscher & Menou (2010). Heng et al. (2011b) and Rauscher & Menou (2012) introduced dual-band or double-grey radiative transfer into hot Jupiter GCMs. Dobbs-Dixon, Cumming & Lin (2010), Dobbs-Dixon et al. (2012), and Dobbs-Dixon & Agol (2013) adapted a fully explicit, non-hydrostatic fluid dynamical solver, albeit with a truncated grid, to study hot Jovian flows and their observational signatures. Mayne et al. (2014a,

b, 2017) adapted a sophisticated Earth weather/climate model with a non-hydrostatic solver and applied it to hot Jupiter atmospheres. Concurrently, Mendonça et al. (2016) introduced a flexible, non-hydrostatic GCM built from scratch (THOR, the model used in this work). Perna, Heng & Pont (2012) used a suite of GCMs to explore the effects of varying stellar irradiation. Liu & Showman (2013) demonstrated the insensitivity of hot Jupiter GCM outcomes to initial conditions. Parmentier, Showman & Lian (2013) studied the interaction between atmospheric dynamics and condensates in hot Jupiter GCMs. Kataria et al. (2015) compared GCM outputs of WASP-43b to emission spectra measured at different orbital phases, an effort that was followed up by Mendonça et al. (2018a). Oreshenko, Heng & Demory (2016) investigated the effects of scattering by condensates in simplified GCMs of Kepler-7b. Komacek & Showman (2016) and Komacek, Showman & Tan (2017) elucidated the mechanism underlying dayside–nightside heat redistribution, building on the work of Showman & Polvani (2010, 2011). Drummond et al. (2018) and Mendonça et al. (2018b) implemented a simplified disequilibrium chemistry scheme known as 'chemical relaxation' (Cooper & Showman 2006) in hot Jovian GCMs, while Steinrueck et al. (2019) focused on the observational consequences of disequilibrium. Drummond et al. (2020) combined two-stream radiative transfer with chemical kinetics into a fully self-consistent hot Jupiter GCM. Meanwhile, several works have focused on flaws of GCM use for hot Jupiters (Thrastarson & Cho 2011; Skinner & Cho 2021). While the vast majority of models show prograde equatorial flow, some have suggested that retrograde flow may be possible (Carone et al. 2020; Mendonça 2020). Sainsbury-Martinez et al. (2019) have explored the role of potential temperature mixing in the atmosphere on the 'radius-inflation' problem using GCM simulations. Lee et al. (2020) used a GCM to study a brown dwarf that straddles the line between hot Jupiters and stars, as it is highly irradiated by a white dwarf companion. Most recently, a wealth of studies have begun to examine the effects of condensates in hot Jupiter atmospheres, both with grey (Roman & Rauscher 2017; Mendonça et al. 2018a; Roman & Rauscher 2019; Roman et al. 2021) and non-grey (Parmentier et al. 2016; Lines et al. 2018, 2019; Parmentier, Showman & Fortney 2021) radiative-transfer.

As summarized in Table 1, most of the GCM studies cited in the preceding paragraph use one of the following GCMs: SPARC/MITgcm (Showman et al. 2009), the IGCM (Menou & Rauscher 2009; Rauscher & Menou 2010, 2012), the FMS (e.g. Held & Suarez 1994; Frierson et al. 2006), the U.K. Met Office UM (Mayne et al. 2014a, b, 2017; Amundsen et al. 2016) or THOR (Mendonça et al. 2016; Deitrick et al. 2020). The computer code of Dobbs-Dixon & Lin (2008), Dobbs-Dixon et al. (2010, 2012), and Dobbs-Dixon & Agol (2013) is unnamed.

The current study builds on this rich body of work on hot Jupiter GCMs by coupling the THOR GCM with the HELIOS radiative transfer solver (Malik et al. 2017, 2019) for the first time, building on the pioneering work of Showman et al. (2009), Amundsen et al. (2016), Mayne et al. (2017), and others.

1.3 Accurate scattering of radiation by medium-sized and large aerosols/condensates

Hot Jupiters are believed to have cloudy/hazy atmospheres (e.g. Pont et al. 2008, 2013; Sing et al. 2016; Stevenson 2016), which motivates the accurate treatment of scattering by aerosols/condensates. The two-stream method of radiative transfer is used extensively in GCMs (Table 1), because of its speed and simplicity of implementation. However, it suffers from a serious shortcoming: it overestimates

Table 1. Selected list of GCMs used for hot Jupiters.

Name of code	Dynamical equations solved	Multiwavelength radiative transfer?	Radiative transfer method	Reference(s)
`SPARC/MITgcm`	Primitive	Yes	Two-stream source function method	Showman et al. (2009)
`IGCM`	Primitive	No[a]	Two-stream	Rauscher & Menou (2010, 2012)
`FMS`	Primitive	No[a]	Two-stream	Heng, Menou & Phillipps (2011a), Heng, Frierson & Phillipps (2011b)
–	Non-hydrostatic Navier-Stokes	Yes[b]	Flux-limited diffusion	Dobbs-Dixon, Agol & Burrows (2012)
–	Non-hydrostatic Navier-Stokes	Yes	Two-stream	Dobbs-Dixon & Agol (2013)
`UM`	Non-hydrostatic Euler	Yes	Two-stream (Edwards–Slingo[c] method)	Mayne et al. (2014a, b, 2017) Amundsen et al. (2016)
`THOR v1`	Non-hydrostatic Euler	No[a]	Two-stream	Mendonça et al. (2016)
`THOR v2`	Non-hydrostatic Euler	No[a]	Two-stream	Deitrick et al. (2020)
`THOR` $+$ `HELIOS`	Non-hydrostatic Euler	Yes	Improved two-stream	Current study

[a]Used dual-band or 'double-grey' radiative transfer that requires the specification of two mean opacities (in the optical and infrared).
[b]Stellar energy deposition is multi-wavelength in implementation, but radiative fluxes are computed using Rosseland mean opacities.
[c]Edwards & Slingo (1996).

the backscattering of radiation caused by medium-sized and large aerosols (Kitzmann, Patzer & Rauer 2013; Heng & Kitzmann 2017). In 1D climate models of early Mars, this artefact has been demonstrated to produce $\sim$50–70 K of artificial warming by the scattering greenhouse effect (Kitzmann 2016). While some GCMs (`SPARC/MITgcm`, `UM`) have implemented more accurate two-stream methods, the effects of different two-stream solutions on hot Jupiter GCMs remain underexplored.

Heng & Kitzmann (2017) and Heng, Malik & Kitzmann (2018) proposed an improved two-stream method of radiative transfer, which removes the artefact of too much backscattering by calibrating the ratio of Eddington coefficients to 32-stream discrete ordinates calculations. Here, we refer to the `HELIOS` solution that uses the backscattering correction as 'improved two-stream' and the `HELIOS` solution without the correction as 'regular two-stream'. In the current study, the improved two-stream method is implemented within a GCM. By comparing the outputs from a pair of GCMs implementing the regular versus improved two-stream methods, we will quantify the error incurred when simulating hot Jupiters. Multiple scattering of radiation is handled using a matrix formulation of the improved two-stream flux solutions, where a tridiagonal matrix is inverted using Thomas's algorithm.

1.4 Structure of paper

The current study is the culmination of a decade of theoretical and computational developments published in more than a dozen papers (Table 2). The foundation of these developments is the first version of `THOR` by Mendonça et al. (2016). As such, a substantial fraction of the current paper is devoted to first concisely reviewing these developments (for self-contained readability) and subsequently integrating them into a single entity. Fig. 1 provides an overview of how the different components of `THOR` $+$ `HELIOS` operate together. Section 2 contains a detailed description of both previous and novel methodology. Section 3 presents 1D comparisons between the new code and the standalone version of `HELIOS` and tests of the spectral convergence. Section 4 presents an illustrative set of four WASP-43b GCMs computed using `THOR` $+$ `HELIOS`. Section 5 provides a summary of the key developments and findings, as well as their implications and opportunities for future work.

Table 2. Legacy of current study.

Development	Reference(s)
GCM benchmark tests	Heng et al. (2011a, b)
Improved two-stream	Heng, Mendonça & Lee (2014), Heng et al. (2018)
radiative transfer theory	Heng & Kitzmann (2017)
Non-hydrostatic dynamical core[a]	Mendonça et al. (2016) Deitrick et al. (2020)
Equilibrium chemistry	Heng & Tsai (2016)
Chemical relaxation[b] (GCM disequilibrium chemistry)	Stock et al. (2018) Tsai et al. (2018) Mendonça et al. (2018b)
Opacities	Grimm & Heng (2015) Grimm et al. (2021)
Temperature–pressure profiles	Heng et al. (2012, 2014)
Two-stream radiative transfer	Malik et al. (2017, 2019)
Cloud properties	Kitzmann & Heng (2018)

[a]In the current study, the terms 'dynamical core' and 'GCM' are used interchangeably, but strictly speaking the former refers only to the core part of the GCM that solves the coupled equations of fluid dynamics.
[b]Results using chemical relaxation are not explicitly shown in the current study, but this capability is already built into `THOR`.

2 METHODOLOGY

2.1 Previous developments

For the current paper to be self-contained, concise reviews of previous codes and techniques are provided, which also give context to the new developments presented. The computer codes are publicly available at https://www.github.com/exoclime.

2.1.1 *THOR general circulation model*

The `THOR` GCM was the first to be developed from scratch for the study of exoplanetary atmospheres (Mendonça et al. 2016), rather than being adapted from GCMs used for Earth or Solar system planets. Unlike most other GCMs used for exoplanets, the dynamical core of `THOR` solves the full set of non-hydrostatic Euler equations, rather than the reduced set of primitive equations of meteorology

THOR+HELIOS
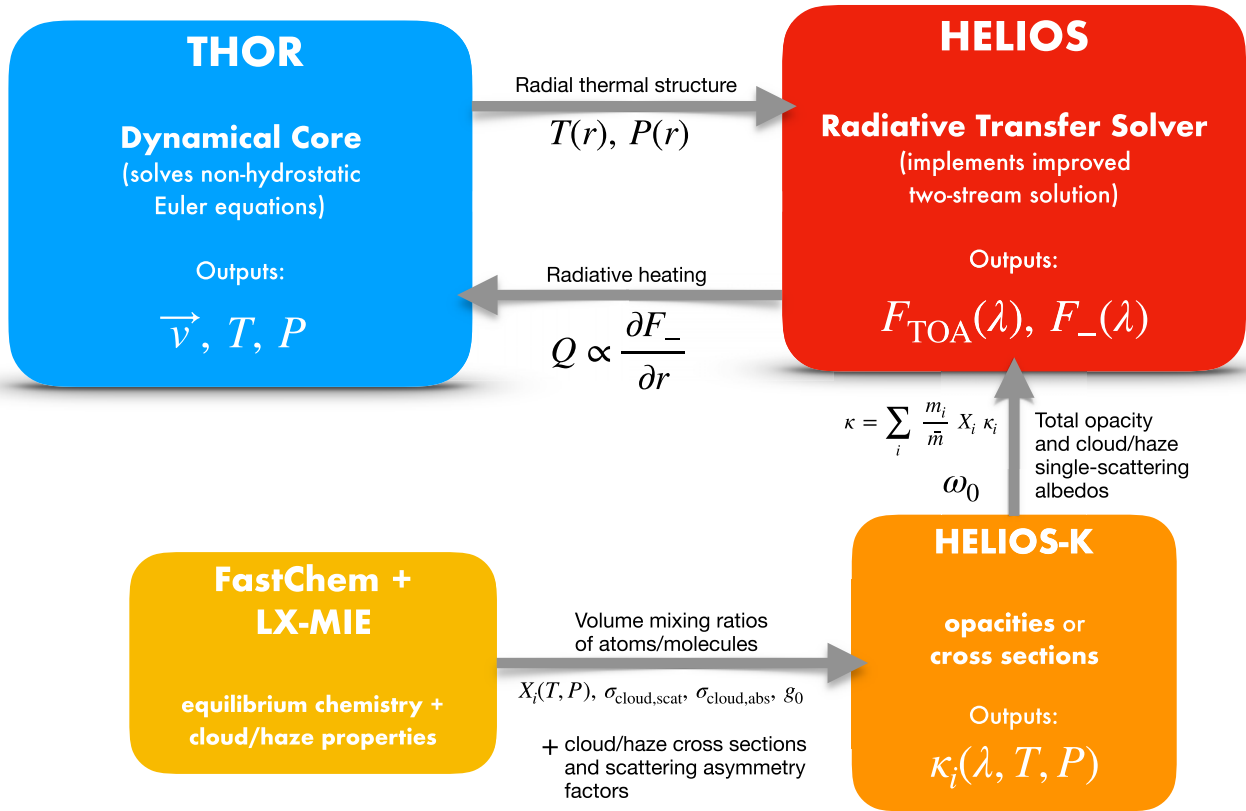## general circulation model

Figure 1. Overview of the THOR + HELIOS general circulation model, which mainly consists of a dynamical core (THOR) and a radiative transfer solver (HELIOS) and is supported by an opacity calculator (HELIOS-K), equilibrium chemistry solver (FastChem) and Mie scattering code (LX-MIE). Given the 3D velocity ($\vec{v}$) and thermal structure ($P(r)$, $T(r)$) provided by THOR, HELIOS performs radiative transfer and computes the radiative net fluxes (F_-) and the flux emerging from the top of the atmosphere (TOA; F_{TOA}). The iteration between THOR and HELIOS solves for a general equilibrium between the 3D atmospheric dynamics and radiative heating, which is more general than the radiative or radiative-convective equilibrium typically computed by 1D radiative transfer codes.

(for a review, see Appendix A). The horizontally explicit vertically implicit (HEVI) algorithm used within THOR and implemented on an icosahedral grid (Fig. 2) with 'spring dynamics' (which allows the pentagons and hexagons of the grid to be projected on to spherical surfaces) is directly taken from the Earth science literature (Satoh 2002, 2003; Tomita & Satoh 2004; Satoh et al. 2008) and first implemented by Mendonça et al. (2016). Following Deitrick et al. (2020), we use a horizontal spatial resolution of the icosahedral grid of $g_{\mathrm{level}} = 4$, which corresponds to an angular resolution of about $4°$ on the sphere. When interpolated on to a latitude–longitude grid, this corresponds to 45 latitude and 90 longitude points. In the vertical/radial direction, the grid has 40 spatial points. It is worth noting that THOR uses MKS physical units to respect the convention of Earth GCMs. The vertical velocity is held at zero at the top and bottom boundaries of the model to conserve mass (Staniforth & Wood 2003). Near the upper boundary, there is a 'sponge-layer', wherein the winds are damped towards their zonal means to mimic wave-breaking and prevent spurious reflections (Jablonowski & Williamson 2011; Mendonça et al. 2018b).

Since THOR is a non-hydrostatic model, acoustic waves are permitted (Tomita & Satoh 2004; Deitrick et al. 2020). However, these waves are very low in energy and have very little impact on circulation (Mendonça et al. 2016). Without using extremely small

time-steps, acoustic waves can be a source of noise, necessitating the use of divergence damping (Tomita & Satoh 2004; Mendonça et al. 2016).

Since hot Jupiter atmospheres can have supersonic winds, it has been suggested that shocks will form along the eastern terminator, where night-side equatorial winds collide with warmer, slower material (Goodman 2009; Dobbs-Dixon et al. 2010; Li & Goodman 2010; Heng 2012). However, 2D shock-capturing simulations in Fromang, Leconte & Heng (2016) suggested that flows on hot Jupiters are smoothly decelerated through the sonic point. The THOR algorithm is not designed to capture shocks, thus we are not prepared to weigh-in on the matter of shocks. The computationally efficient, shock-capturing 3D GCM introduced in Ge et al. (2020) may be well suited to address this issue.

2.1.2 *HELIOS radiative transfer code*

The HELIOS radiative transfer code (Malik et al. 2017) is based on implementing the workhorse two-stream method (Schuster 1905; Meador & Weaver 1980; Toon et al. 1989; Pierrehumbert 2010; Heng et al. 2014). A later version of the code (Malik et al. 2019) implemented the improved two-stream radiative transfer method

(Heng & Kitzmann 2017; Heng et al. 2018) and dry convective adjustment (Manabe, Smagorinsky & Strickler 1965). Equilibrium chemistry is computed using the `FastChem` code (Stock et al. 2018). When used on its own, `HELIOS` performs an iteration to solve for radiative-convective equilibrium given assumptions about the chemistry of the atmosphere and its initial temperature–pressure profile. When used in tandem with the `THOR` GCM, the iteration for radiative-convective equilibrium is deactivated. This is because `THOR` iterates for a more general equilibrium between the 3D atmospheric dynamics and radiative heating. Given a temperature–pressure profile supplied by `THOR`, `HELIOS` computes the radiative fluxes associated with heating/cooling, which are subsequently used to update the temperature–pressure profile (Fig. 1).

The original `HELIOS` code was written using both the `Python` and `CUDA C++` programming languages. In order to perform the coupling to `THOR` without suffering a computational bottleneck, another version of `HELIOS` was written in C++; it is internally named `Alfrodull` for book-keeping purposes.[1] It is worth noting that the original `HELIOS` code uses CGS physical units, whereas `Alfrodull` uses MKS physical units to be consistent with `THOR`.

Malik et al. (2017) benchmarked the `HELIOS` code against Miller-Ricci & Fortney (2010), finding that results for GJ 1214b compared well between the two models, both in the temperature–pressure profile and the spectrum. The T–P profile was produced using k-tables and the spectrum was produced using high-resolution opacity sampling. Further validation of `HELIOS` against other codes utilizing correlated-k, `Exo-REM` (Baudino et al. 2015), `petitCODE` (Mollière et al. 2015), and ATMO (Amundsen et al. 2014), was provided in Malik et al. (2019).

2.1.3 `HELIOS-K`: atmospheric opacity calculator

Atmospheric opacities (cross-sections per unit mass) are calculated using the `HELIOS-K` calculator (Grimm & Heng 2015; Grimm et al. 2021). Drawing from the `HITEMP` and `ExoMol` spectroscopic data bases, we include contributions from several major carbon, oxygen, nitrogen, and sulphur carriers: H_2O (Polyansky et al. 2018), CO (Li et al. 2015), CO_2 (Rothman et al. 2010), CH_4 (Yurchenko et al. 2013; Yurchenko & Tennyson 2014), NH_3 (Yurchenko, Barber & Tennyson 2011), HCN (Harris et al. 2006; Barber et al. 2014), C_2H_2 (Chubb, Tennyson & Yurchenko 2020), PH_3 (Sousa-Silva et al. 2015), and H_2S (Azzam et al. 2016). We also include collision-induced absorption due to H_2–H_2 (Abel et al. 2011) and H_2–He (Abel et al. 2012) pairs. Truncated Voigt profiles with a line-wing cutoff of 100 cm^{-1} are assumed. Pressure broadening is included using standard broadening parameters provided by `HITEMP` and `ExoMol`. All of the opacities used are publicly available at https://dace.unige.ch/.

For integration of the GCM, we utilize k-distributions with 30 bins, equally spaced in wavenumber from 0.3 μm to 200 μm. We construct k-tables using the opacities sampled at the native resolution of `HELIOS-K`, which has a spacing in wavenumber of $\delta \nu = 0.01$ cm^{-1}. For this study, the k-table bins are equal size in wavenumber, and we use 30 bins (but see Section 3). The high-resolution opacities are combined (i.e. pre-mixed), across temperature ($50 \leq T \leq 3000$ K; 60 values) and pressure ($10^{-6} \leq P \leq 10^3$ bar; 28 values equally spaced in $\log P$), assuming chemical equilibrium and a metallicity of [Fe/H] =
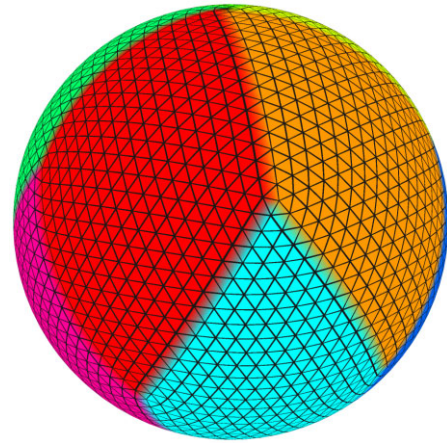
Figure 2. Icosahedral grid used in `THOR`. Each rhomboid represents regions on the grid that map to a square array of points, linearly stored in memory. Equations for points on a rhomboid are evaluated as a block in parallel on one core per point on the GPU. This partitioning into memory chunks allows the GPU to parallelize operations on the grid more efficiently by requiring fewer memory access operations.

−0.13 (the metallicity of the host star; Sousa et al. 2018). Equilibrium chemistry calculations are performed using the `FastChem` code (Stock et al. 2018). Finally, within each bin, the resulting opacities are sorted and interpolated on to 20 Gaussian points (see equations 33 and 34 of Malik et al. 2017). Post-processing uses opacity sampling with a spectral resolution of 500, which corresponds to 3255 wavelength points. Spectral resolution is defined here to be

$$R = \frac{\lambda}{\Delta \lambda}, \tag{1}$$

which results in a logarithmic spacing of samples.

2.1.4 `LX-MIE` Mie scattering code: cloud/haze properties

To include the effects of clouds or hazes, one needs to compute the absorption and scattering cross-sections of their constituent particles, as well as the scattering asymmetry factors (which describe how anisotropic or isotropic the scattered radiation is). To this end, we use the `LX-MIE` Mie scattering code (Kitzmann & Heng 2018). We are agnostic about the formation mechanism of these constituent particles and term them 'aerosols' or 'condensates'. For the current study, these terms are used synonymously, because we do not attempt to model cloud or haze formation and only include their absorption and scattering effects on the radiative transfer.

2.1.5 `PHOENIX` stellar template

In the current study, we focus on the hot Jupiter WASP-43b (Hellier et al. 2011; Gillon et al. 2012). To model the stellar radiation incident upon this gas-giant exoplanet, we use stellar templates from the `PHOENIX` library (Husser et al. 2013). To interpolate for the stellar template of WASP-43, we use the following values of the stellar properties (Sousa et al. 2018): $T_\star = 4798$ K, $\log g_\star = 4.55$ (cgs units), [Fe/H] = −0.13. Given the lack of information, the alpha element enhancement is assumed to be solar. For integration, we average the `PHOENIX` template over the opacity k-table bins, while for post-processing, we use opacity sampling at resolution $R = 500$. Fig. 3 shows the final stellar template used.
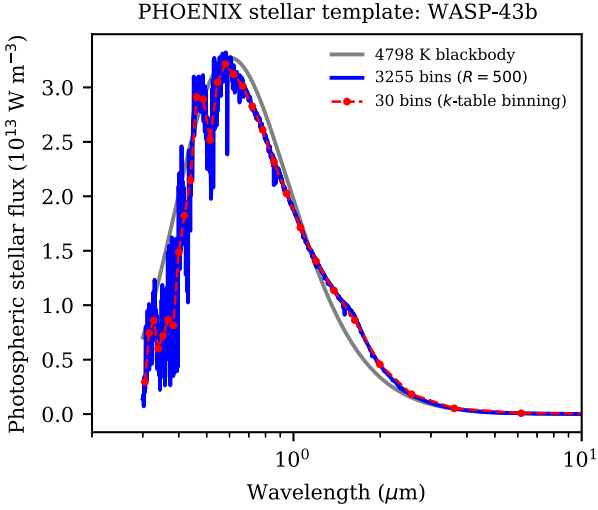
Figure 3. PHOENIX stellar template of WASP-43 interpolated at two different spectral resolutions. A 4798 K blackbody is shown for comparison. The blue curve is the high-resolution ($R = 500$) spectrum used for post-processing. The red curve shows the spectrum used for integration; this spectrum is constructed from the original PHOENIX template by averaging the flux over each k-table bin (used for the opacities; see Section 2.1.3). The red points indicate the centres of the k-table bins.

2.2 New developments: THOR + HELIOS

2.2.1 Model grid, radiative transfer equations and boundary conditions

THOR + HELIOS uses a staggered radial/vertical grid that is inherited from HELIOS. It has two variants: isothermal and non-isothermal layers (Fig. 4), which correspond to whether only a constant Planck function is assumed or its gradient is additionally computed, respectively (Heng et al. 2014; Malik et al. 2017). The temperature and pressure at the center of each isothermal layer are provided by THOR, which are then used to compute the opacities, single-scattering albedos, mean molecular mass, Planck function, etc. The stellar beam and diffuse fluxes exist only at the interfaces of each layer and are computed by HELIOS. For non-isothermal layers, each layer is divided into upper and lower sub-layers (Mendonça et al. 2015; Malik et al. 2017, 2019). While temperatures and pressures at the centre of the layer are already defined by the dynamical core, the values at the interfaces are determined by linear interpolation. Fluxes are defined at the interfaces and at the layer centers. The values of the opacities, single-scattering albedos, mean molecular mass, Planck function, etc, are computed at both layer centres and interfaces; their values in the upper and lower sub-layers are taken to be the arithmetic mean of their central and interface values.

Appendix B reviews and re-casts the improved two-stream flux solutions of Heng et al. (2018) mostly in the notation of Malik et al. (2019), which is the form implemented in the HELIOS code. Consider an isothermal layer with centre index $i - 1$ and interface indices $i - 1$ (lower interface) and i (upper interface), as shown in Fig. 4. The outgoing (upward) flux at the upper interface is

$$
\begin{aligned}
\chi_{i-1} F_{\uparrow i} = {} & \psi_{i-1} F_{\uparrow i-1} - \xi_{i-1} F_{\downarrow i} \\
& + \Pi_{i-1} B_{i-1} (\chi_{i-1} + \xi_{i-1} - \psi_{i-1}) \\
& + \psi_{i-1} \mathcal{G}_{+,i-1} F_{\text{beam},i-1} \\
& - \left(\xi_{i-1} \mathcal{G}_{-,i-1} + \chi_{i-1} \mathcal{G}_{+,i-1} \right) F_{\text{beam},i}.
\end{aligned} \tag{2}
$$

The incoming (downward) flux at the lower interface is

$$
\begin{aligned}
\chi_{i-1} F_{\downarrow i-1} = {} & \psi_{i-1} F_{\downarrow i} - \xi_{i-1} F_{\uparrow i-1} \\
& + \Pi_{i-1} B_{i-1} (\chi_{i-1} + \xi_{i-1} - \psi_{i-1}) \\
& + \psi_{i-1} \mathcal{G}_{-,i-1} F_{\text{beam},i} \\
& - \left(\xi_{i-1} \mathcal{G}_{+,i-1} + \chi_{i-1} \mathcal{G}_{-,i-1} \right) F_{\text{beam},i-1}.
\end{aligned} \tag{3}
$$

For non-isothermal layers, the Planck function varies over the layer and it has a non-zero gradient with respect to the optical depth. There are now four expressions for the fluxes (Fig. 4). Quantities at the centre of each layer are superscripted by '(c)'; in the upper and lower sub-layers, they are superscripted by '(upper)' and '(lower)', respectively. The outgoing (upward) flux at the upper interface is

$$
\begin{aligned}
\chi_{i-1}^{(\text{upper})} F_{\uparrow i} = {} & \psi_{i-1}^{(\text{upper})} F_{\uparrow i-1}^{(c)} - \xi_{i-1}^{(\text{upper})} F_{\downarrow i} \\
& + \Pi_{i-1}^{(\text{upper})} B_i \left(\chi_{i-1}^{(\text{upper})} + \xi_{i-1}^{(\text{upper})} \right) \\
& - \Pi_{i-1}^{(\text{upper})} \psi_{i-1}^{(\text{upper})} B_{i-1}^{(c)} \\
& + \Pi_{i-1}^{(\text{upper})} \frac{B_{i-1}^{(c)} - B_i}{\tau_{i-1}^{(c)} - \tau_i} \Theta_{i-1}^{(\text{upper})} \\
& + \psi_{i-1}^{(\text{upper})} \mathcal{G}_{+,i-1}^{(\text{upper})} F_{\text{beam},i-1}^{(c)} \\
& - \left(\xi_{i-1}^{(\text{upper})} \mathcal{G}_{-,i-1}^{(\text{upper})} + \chi_{i-1}^{(\text{upper})} \mathcal{G}_{+,i-1}^{(\text{upper})} \right) F_{\text{beam},i}.
\end{aligned} \tag{4}
$$

where we have defined

$$
\begin{aligned}
\Theta_{i-1}^{(\text{upper})} \equiv {} & \frac{1}{2 E_{i-1}^{(\text{upper})} \left(1 - \omega_{0,i-1}^{(\text{upper})} g_{0,i-1}^{(\text{upper})} \right)} \\
& \times \left(\chi_{i-1}^{(\text{upper})} - \psi_{i-1}^{(\text{upper})} - \xi_{i-1}^{(\text{upper})} \right).
\end{aligned} \tag{5}
$$

If $(\tau_{i-1}^{(c)} - \tau_i) < e_\tau$, then the gradient of the Planck function (fourth line of equation 4) is set to zero and the Planck functions (second and third lines of equation 4) are replaced by $(B_{i-1}^{(c)} + B_i)/2$. The tolerance $e_\tau = 10^{-4}$ allows a non-isothermal layer to become an isothermal one when the optical depth of the layer is too small and ensures numerical stability. The incoming (downward) flux at the centre of the layer also uses quantities from the upper sub-layer,

$$
\begin{aligned}
\chi_{i-1}^{(\text{upper})} F_{\downarrow i-1}^{(c)} = {} & \psi_{i-1}^{(\text{upper})} F_{\downarrow i} - \xi_{i-1}^{(\text{upper})} F_{\uparrow i-1}^{(c)} \\
& + \Pi_{i-1}^{(\text{upper})} B_{i-1}^{(c)} \left(\chi_{i-1}^{(\text{upper})} + \xi_{i-1}^{(\text{upper})} \right) \\
& - \Pi_{i-1}^{(\text{upper})} \psi_{i-1}^{(\text{upper})} B_i \\
& - \Pi_{i-1}^{(\text{upper})} \frac{B_{i-1}^{(c)} - B_i}{\tau_{i-1}^{(c)} - \tau_i} \Theta_{i-1}^{(\text{upper})} \\
& + \psi_{i-1}^{(\text{upper})} \mathcal{G}_{-,i-1}^{(\text{upper})} F_{\text{beam},i} \\
& - \left(\xi_{i-1}^{(\text{upper})} \mathcal{G}_{+,i-1}^{(\text{upper})} + \chi_{i-1}^{(\text{upper})} \mathcal{G}_{-,i-1}^{(\text{upper})} \right) F_{\text{beam},i-1}^{(c)}.
\end{aligned} \tag{6}
$$

The other two fluxes use quantities from the lower sub-layer. The outgoing (upward) flux at the centre of the layer is

$$
\begin{aligned}
\chi_{i-1}^{(\text{lower})} F_{\uparrow i-1}^{(c)} = {} & \psi_{i-1}^{(\text{lower})} F_{\uparrow i-1} - \xi_{i-1}^{(\text{lower})} F_{\downarrow i-1}^{(c)} \\
& + \Pi_{i-1}^{(\text{lower})} B_{i-1}^{(c)} \left(\chi_{i-1}^{(\text{lower})} + \xi_{i-1}^{(\text{lower})} \right) \\
& - \Pi_{i-1}^{(\text{lower})} \psi_{i-1}^{(\text{lower})} B_{i-1} \\
& + \Pi_{i-1}^{(\text{lower})} \frac{B_{i-1} - B_{i-1}^{(c)}}{\tau_{i-1} - \tau_{i-1}^{(c)}} \Theta_{i-1}^{(\text{lower})} \\
& + \psi_{i-1}^{(\text{lower})} \mathcal{G}_{+,i-1}^{(\text{lower})} F_{\text{beam},i-1} \\
& - \left(\xi_{i-1}^{(\text{lower})} \mathcal{G}_{-,i-1}^{(\text{lower})} + \chi_{i-1}^{(\text{lower})} \mathcal{G}_{+,i-1}^{(\text{lower})} \right) F_{\text{beam},i-1}^{(c)},
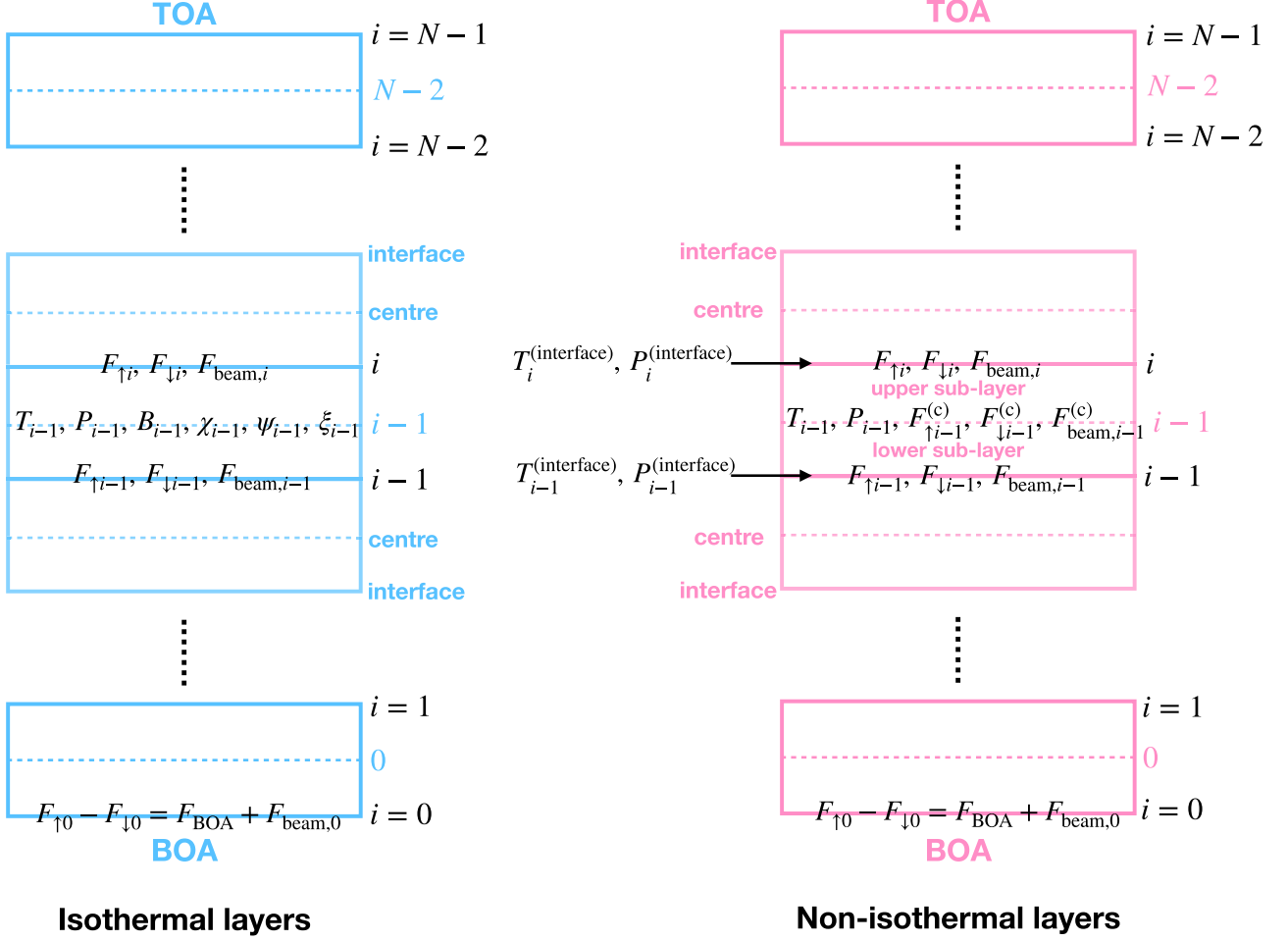\end{aligned} \tag{7}
$$

Figure 4. Schematics of the staggered radial/vertical grid used in the `THOR + HELIOS` general circulation model. The schematic on the left is for isothermal layers, where the temperature, pressure, Planck function, etc, are defined only at the centre of each layer. Both the stellar beam and diffuse fluxes exist only at the interfaces. The schematic on the right is for non-isothermal layers (non-constant Planck function), which are each divided into upper and lower sub-layers. Temperatures, pressures, fluxes, etc, exist at both the centre of each layer and its interfaces. Quantities within each sub-layer take on values that are the average of the centre and interface. TOA and BOA are acronyms for top and bottom of atmosphere, respectively.

where we have defined

$$
\Theta_{i-1}^{(\text{lower})} \equiv \frac{1}{2 E_{i-1}^{(\text{lower})} \left(1 - \omega_{0,i-1}^{(\text{lower})} g_{0,i-1}^{(\text{lower})} \right)}
$$
$$
\times \left(\chi_{i-1}^{(\text{lower})} - \psi_{i-1}^{(\text{lower})} - \xi_{i-1}^{(\text{lower})} \right). \quad (8)
$$

If $(\tau_{i-1} - \tau_{i-1}^{(c)}) < e_\tau$, then the gradient of the Planck function (fourth line of equation 7) is set to zero and the Planck functions (second and third lines of equation 7) are replaced by $(B_{i-1} + B_{i-1}^{(c)})/2$. Finally, the incoming (downward) flux at the lower interface is

$$
\chi_{i-1}^{(\text{lower})} F_{\downarrow i-1} = \psi_{i-1}^{(\text{lower})} F_{\downarrow i-1}^{(c)} - \xi_{i-1}^{(\text{lower})} F_{\uparrow i-1}
$$
$$
+ \Pi_{i-1}^{(\text{lower})} B_{i-1} \left(\chi_{i-1}^{(\text{lower})} + \xi_{i-1}^{(\text{lower})} \right)
$$
$$
- \Pi_{i-1}^{(\text{lower})} \psi_{i-1}^{(\text{lower})} B_{i-1}^{(c)}
$$
$$
- \Pi_{i-1}^{(\text{lower})} \frac{B_{i-1} - B_{i-1}^{(c)}}{\tau_{i-1} - \tau_{i-1}^{(c)}} \Theta_{i-1}^{(\text{lower})}
$$
$$
+ \psi_{i-1}^{(\text{lower})} \mathcal{G}_{-,i-1}^{(\text{lower})} F_{\text{beam},i-1}^{(c)}
$$
$$
- \left(\xi_{i-1}^{(\text{lower})} \mathcal{G}_{+,i-1}^{(\text{lower})} + \chi_{i-1}^{(\text{lower})} \mathcal{G}_{-,i-1}^{(\text{lower})} \right) F_{\text{beam},i-1}. \quad (9)
$$

Heating of the atmosphere by the stellar beam is given by equation (B6), which is essentially Beer's law applied in the shortwave. Operationally, the flux associated with the stellar beam is added to the downward flux before the net flux is computed. As the stellar beam is attenuated, it becomes diffuse emission. At the top boundary of the atmosphere, the direct beam enters at full strength; the upward stream of the diffuse beam escapes to space. At the bottom of the atmosphere (BOA), the boundary condition is

$$
F_{\uparrow 0} - F_{\downarrow 0} = F_{\text{BOA}} + F_{\text{beam},0}, \quad (10)
$$

where $F_{\text{BOA}} = \pi B(T_{\text{int}})$, B is the Planck function and T_{int} is the interior temperature. If the stellar beam is not attenuated at the BOA, then we have $F_{\text{beam},0} \neq 0$ and it is artificially reflected upwards as part of the BOA boundary condition. Examining the profile of $F_{\text{beam},i}$ with radial distance is a sanity check to ensure that the BOA is located at a sufficiently deep pressure and/or if the adequate opacity sources have been included such that the model atmosphere is not implausibly transparent to starlight.

Figure 5. Matrix form of the improved two-stream solutions of radiative transfer in the THOR + HELIOS general circulation model. The 2×1 matrix $\hat{X}$, which contains the outgoing and incoming fluxes, may be obtained using the Thomas's algorithm (see text for details), where the tridiagonal matrix operating on $\hat{X}$ is composed of elements $\hat{A}$, $\hat{B}$, and $\hat{C}$ that are 2×2 matrices. The F_{TOA} term refers to the diffuse infrared emission (and *not* the stellar beam) at the top of the atmosphere, which is normally set to zero; it is available in the THOR + HELIOS code as an option for testing. For exoplanets without surfaces, we set $F_{\text{BOA}} = 0$ as interior heating is included elsewhere in the algorithm.

Inspection of equation (B8) reveals that there exists a critical value of $\mu_\star$ for which $\mathcal{G}_\pm$ diverges,

$$\mu_{\star,\text{crit}} = \frac{1}{2\sqrt{E\,(E - \omega_0)(1 - \omega_0 g_0)}}. \tag{11}$$

This issue has previously been noted and addressed by Toon et al. (1989), who proposed that 'this problem can be eliminated by simply choosing a slightly different value of $\mu_\star$'. In the 3D simulations, this singularity is highly likely to appear and using this proposed solution can lead to unphysical forcing patterns. Instead, we perform a check on term associated with $\mathcal{G}_\pm$, $4E\mu_\star^2(E - \omega_0)(1 - \omega_0 g_0) - 1$. It can be shown that as $\mu_\star$ approaches the critical value, this term reduces to $2\mu_\star$. In the case that the full term is less than 10^{-5}, we switch to this reduced form. It is not clear what the tolerance should be here; we have chosen a value that avoids the singularity effectively without causing unusual behaviour.

2.2.2 Multiple scattering using Thomas's algorithm

The improved two-stream flux solutions, described in Appendix B, allow for radiation from an atmospheric layer to be scattered to its immediate neighbours. In the absence of scattering, the arrays of outgoing and incoming fluxes may be computed independently of each other, because they depend only on the fluxes impinging upon the bottom and top of each layer, respectively. When scattering is present, the outgoing or incoming flux of each layer now depends

on both boundary conditions. One may use an iterative approach to populate these flux arrays (Oreshenko et al. 2016).

When the calculation is repeated, radiation is scattered twice and may propagate across two layers. When repeated $\mathcal{N}$ times, radiation is scattered $\mathcal{N}$ times in both directions – the multiple scattering of radiation in a model atmosphere. The simplest implementation of multiple scattering is simply to iterate the two-stream solutions, across the entire atmosphere, for a finite number of times. This is the approach adopted in the stand-alone HELIOS code; Malik et al. (2019) performed $\mathcal{N} = 200$ iterations for multiple scattering. The simplified GCMs of Oreshenko et al. (2016) also used this approach, typically enforcing ~10 iterations.

Instead of iterating pairwise through the entire atmosphere, a better approach is to cast the entire set of two-stream flux solutions in matrix form (Fig. 5) and solve the system by matrix inversion. This approach has been used in numerous radiative-transfer models since its introduction in Toon et al. (1989). We include a complete description of the method here since it is a new addition to the HELIOS model.

The matrices themselves contain 2×2 and 2×1 sub-matrices, which obey the following relation:

$$\hat{A}_i\hat{X}_{i-1} + \hat{B}_i\hat{X}_i + \hat{C}_i\hat{X}_{i+1} = \hat{D}_i, \tag{12}$$

where the 2×1 sub-matrix $\hat{X}$ contains the outgoing and incoming fluxes. The 2×2 sub-matrices $\hat{A}$, $\hat{B}$, and $\hat{C}$ contain the coefficients χ, ξ, and ψ (see equation B1 for definitions). The 2×1 sub-matrix $\hat{D}$ contains the blackbody and stellar beam terms. Solving

$$
\begin{pmatrix}
1 & -1 & 0 & 0 & 0 & 0 & \ldots & 0 & 0 & 0 & 0 & 0 & 0 & 0 & 0 & 0 & 0 & 0 & 0 \\
\xi_0^{(\mathrm{lower})} & \chi_0^{(\mathrm{lower})} & 0 & -\psi_0^{(\mathrm{lower})} & 0 & 0 & \ldots & 0 & 0 & 0 & 0 & 0 & 0 & 0 & 0 & 0 & 0 & 0 & 0 \\
-\psi_0^{(\mathrm{lower})} & 0 & \chi_0^{(\mathrm{lower})} & \xi_0^{(\mathrm{lower})} & 0 & 0 & \ldots & 0 & 0 & 0 & 0 & 0 & 0 & 0 & 0 & 0 & 0 & 0 & 0 \\
0 & 0 & \xi_0^{(\mathrm{upper})} & \chi_0^{(\mathrm{upper})} & 0 & -\psi_0^{(\mathrm{upper})} & \ldots & 0 & 0 & 0 & 0 & 0 & 0 & 0 & 0 & 0 & 0 & 0 & 0 \\
\ldots & \ldots & \ldots & \ldots & \ldots & \ldots & & \ldots & \ldots & \ldots & \ldots & \ldots & \ldots & \ldots & \ldots & \ldots & \ldots & \ldots & \ldots \\
0 & 0 & 0 & 0 & 0 & 0 & \ldots & -\psi_{i-2}^{(\mathrm{upper})} & 0 & \chi_{i-2}^{(\mathrm{upper})} & \xi_{i-2}^{(\mathrm{upper})} & 0 & 0 & 0 & 0 & 0 & 0 & 0 & 0 \\
0 & 0 & 0 & 0 & 0 & 0 & \ldots & 0 & 0 & \xi_{i-1}^{(\mathrm{lower})} & \chi_{i-1}^{(\mathrm{lower})} & 0 & -\psi_{i-1}^{(\mathrm{lower})} & 0 & 0 & 0 & 0 & 0 & 0 \\
0 & 0 & 0 & 0 & 0 & 0 & \ldots & 0 & 0 & -\psi_{i-1}^{(\mathrm{lower})} & 0 & \chi_{i-1}^{(\mathrm{lower})} & \xi_{i-1}^{(\mathrm{lower})} & 0 & 0 & 0 & 0 & 0 & 0 \\
0 & 0 & 0 & 0 & 0 & 0 & \ldots & 0 & 0 & 0 & 0 & \xi_{i-1}^{(\mathrm{upper})} & \chi_{i-1}^{(\mathrm{upper})} & 0 & -\psi_{i-1}^{(\mathrm{upper})} & 0 & 0 & 0 & 0 \\
0 & 0 & 0 & 0 & 0 & 0 & \ldots & 0 & 0 & 0 & 0 & -\psi_{i-1}^{(\mathrm{upper})} & 0 & \chi_{i-1}^{(\mathrm{upper})} & \xi_{i-1}^{(\mathrm{upper})} & 0 & 0 & 0 & 0 \\
\ldots & \ldots & \ldots & \ldots & \ldots & \ldots & & \ldots & \ldots & \ldots & \ldots & \ldots & \ldots & \ldots & \ldots & \ldots & \ldots & \ldots & \ldots \\
0 & 0 & 0 & 0 & 0 & 0 & \ldots & 0 & 0 & 0 & 0 & 0 & 0 & \ldots & -\psi_{N-2} & 0 & \chi_{N-2} & \xi_{N-2} \\
0 & 0 & 0 & 0 & 0 & 0 & \ldots & 0 & 0 & 0 & 0 & 0 & 0 & \ldots & 0 & 0 & 0 & 1
\end{pmatrix}
\begin{pmatrix}
F_{\uparrow 0} \\ F_{\downarrow 0} \\ F_{\uparrow 0}^{(c)} \\ F_{\downarrow 0}^{(c)} \\ \vdots \\ F_{\uparrow i-1} \\ F_{\downarrow i-1} \\ F_{\uparrow i-1}^{(c)} \\ F_{\downarrow i-1}^{(c)} \\ F_{\uparrow i} \\ F_{\downarrow i} \\ \vdots \\ F_{\uparrow N-1} \\ F_{\downarrow N-1}
\end{pmatrix}
$$

$$
=
\begin{pmatrix}
F_{\mathrm{BOA}} + F_{\mathrm{beam},0} \\[4pt]
\Pi_0^{(\mathrm{lower})} B_0 \left(\chi_0^{(\mathrm{lower})} + \xi_0^{(\mathrm{lower})}\right) - \Pi_0^{(\mathrm{lower})} B_0^{(c)} \psi_0^{(\mathrm{lower})} - \Pi_0^{(\mathrm{lower})} \frac{B_0 - B_0^{(c)}}{\tau_0 - \tau_0^{(c)}} \Theta_0^{(\mathrm{lower})} + \psi_0^{(\mathrm{lower})} \mathscr{G}_{-,0}^{(\mathrm{lower})} F_{\mathrm{beam},0}^{(c)} - \left(\xi_0^{(\mathrm{lower})} \mathscr{G}_{+,0}^{(\mathrm{lower})} + \chi_0^{(\mathrm{lower})} \mathscr{G}_{-,0}^{(\mathrm{lower})}\right) F_{\mathrm{beam},0} \\[4pt]
\Pi_0^{(\mathrm{lower})} B_0^{(c)} \left(\chi_0^{(\mathrm{lower})} + \xi_0^{(\mathrm{lower})}\right) - \Pi_0^{(\mathrm{lower})} B_0 \psi_0^{(\mathrm{lower})} - \Pi_0^{(\mathrm{lower})} \frac{B_0 - B_0^{(c)}}{\tau_0 - \tau_0^{(c)}} \Theta_0^{(\mathrm{lower})} + \psi_0^{(\mathrm{lower})} \mathscr{G}_{+,0}^{(\mathrm{lower})} F_{\mathrm{beam},0} - \left(\xi_0^{(\mathrm{lower})} \mathscr{G}_{-,0}^{(\mathrm{lower})} + \chi_0^{(\mathrm{lower})} \mathscr{G}_{+,0}^{(\mathrm{lower})}\right) F_{\mathrm{beam},0}^{(c)} \\[4pt]
\Pi_0^{(\mathrm{upper})} B_0^{(c)} \left(\chi_0^{(\mathrm{upper})} + \xi_0^{(\mathrm{upper})}\right) - \Pi_0^{(\mathrm{upper})} B_1 \psi_0^{(\mathrm{upper})} - \Pi_0^{(\mathrm{upper})} \frac{B_0^{(c)} - B_1}{\tau_0^{(c)} - \tau_1} \Theta_0^{(\mathrm{upper})} + \psi_0^{(\mathrm{upper})} \mathscr{G}_{-,0}^{(\mathrm{upper})} F_{\mathrm{beam},1} - \left(\xi_0^{(\mathrm{upper})} \mathscr{G}_{+,0}^{(\mathrm{upper})} + \chi_0^{(\mathrm{upper})} \mathscr{G}_{-,0}^{(\mathrm{upper})}\right) F_{\mathrm{beam},0}^{(c)} \\[4pt]
\vdots \\[4pt]
\Pi_{i-1}^{(\mathrm{lower})} B_{i-1} \left(\chi_{i-1}^{(\mathrm{lower})} + \xi_{i-1}^{(\mathrm{lower})}\right) - \Pi_{i-1}^{(\mathrm{lower})} \psi_{i-1}^{(\mathrm{lower})} B_{i-1}^{(c)} - \Pi_{i-1}^{(\mathrm{lower})} \frac{B_{i-1} - B_{i-1}^{(c)}}{\tau_{i-1} - \tau_{i-1}^{(c)}} \Theta_{i-1}^{(\mathrm{lower})} + \psi_{i-1}^{(\mathrm{lower})} \mathscr{G}_{-,i-1}^{(\mathrm{lower})} F_{\mathrm{beam},i-1}^{(c)} - \left(\xi_{i-1}^{(\mathrm{lower})} \mathscr{G}_{+,i-1}^{(\mathrm{lower})} + \chi_{i-1}^{(\mathrm{lower})} \mathscr{G}_{-,i-1}^{(\mathrm{lower})}\right) F_{\mathrm{beam},i-1} \\[4pt]
\Pi_{i-1}^{(\mathrm{lower})} B_{i-1}^{(c)} \left(\chi_{i-1}^{(\mathrm{lower})} + \xi_{i-1}^{(\mathrm{lower})}\right) - \Pi_{i-1}^{(\mathrm{lower})} \psi_{i-1}^{(\mathrm{lower})} B_{i-1} + \Pi_{i-1}^{(\mathrm{lower})} \frac{B_{i-1} - B_{i-1}^{(c)}}{\tau_{i-1} - \tau_{i-1}^{(c)}} \Theta_{i-1}^{(\mathrm{lower})} + \psi_{i-1}^{(\mathrm{lower})} \mathscr{G}_{+,i-1}^{(\mathrm{lower})} F_{\mathrm{beam},i-1} - \left(\xi_{i-1}^{(\mathrm{lower})} \mathscr{G}_{-,i-1}^{(\mathrm{lower})} + \chi_{i-1}^{(\mathrm{lower})} \mathscr{G}_{+,i-1}^{(\mathrm{lower})}\right) F_{\mathrm{beam},i-1}^{(c)} \\[4pt]
\Pi_{i-1}^{(\mathrm{upper})} B_{i-1}^{(c)} \left(\chi_{i-1}^{(\mathrm{upper})} + \xi_{i-1}^{(\mathrm{upper})}\right) - \Pi_{i-1}^{(\mathrm{upper})} \psi_{i-1}^{(\mathrm{upper})} B_i - \Pi_{i-1}^{(\mathrm{upper})} \frac{B_{i-1}^{(c)} - B_i}{\tau_{i-1}^{(c)} - \tau_i} \Theta_{i-1}^{(\mathrm{upper})} + \psi_{i-1}^{(\mathrm{upper})} \mathscr{G}_{-,i-1}^{(\mathrm{upper})} F_{\mathrm{beam},i} - \left(\xi_{i-1}^{(\mathrm{upper})} \mathscr{G}_{+,i-1}^{(\mathrm{upper})} + \chi_{i-1}^{(\mathrm{upper})} \mathscr{G}_{-,i-1}^{(\mathrm{upper})}\right) F_{\mathrm{beam},i-1}^{(c)} \\[4pt]
\Pi_{i-1}^{(\mathrm{upper})} B_i \left(\chi_{i-1}^{(\mathrm{upper})} + \xi_{i-1}^{(\mathrm{upper})}\right) - \Pi_{i-1}^{(\mathrm{upper})} \psi_{i-1}^{(\mathrm{upper})} B_{i-1}^{(c)} + \Pi_{i-1}^{(\mathrm{upper})} \frac{B_{i-1}^{(c)} - B_i}{\tau_{i-1}^{(c)} - \tau_i} \Theta_{i-1}^{(\mathrm{upper})} + \psi_{i-1}^{(\mathrm{upper})} \mathscr{G}_{+,i-1}^{(\mathrm{upper})} F_{\mathrm{beam},i-1}^{(c)} - \left(\xi_{i-1}^{(\mathrm{upper})} \mathscr{G}_{-,i-1}^{(\mathrm{upper})} + \chi_{i-1}^{(\mathrm{upper})} \mathscr{G}_{+,i-1}^{(\mathrm{upper})}\right) F_{\mathrm{beam},i} \\[4pt]
\vdots \\[4pt]
\Pi_{N-2}^{(\mathrm{upper})} B_{N-2}^{(c)} \left(\chi_{N-2}^{(\mathrm{upper})} + \xi_{N-2}^{(\mathrm{upper})}\right) - \Pi_{N-2}^{(\mathrm{upper})} \psi_{N-2}^{(\mathrm{upper})} B_{N-1} - \Pi_{N-2}^{(\mathrm{upper})} \frac{B_{N-2}^{(c)} - B_{N-1}}{\tau_{N-2}^{(c)} - \tau_{N-1}} \Theta_{N-2}^{(\mathrm{upper})} + \psi_{N-2}^{(\mathrm{upper})} \mathscr{G}_{-,N-2}^{(\mathrm{upper})} F_{\mathrm{beam},N-1} - \left(\xi_{N-2}^{(\mathrm{upper})} \mathscr{G}_{+,N-2}^{(\mathrm{upper})} + \chi_{N-2}^{(\mathrm{upper})} \mathscr{G}_{-,N-2}^{(\mathrm{upper})}\right) F_{\mathrm{beam},N-2}^{(c)} \\[4pt]
F_{\mathrm{TOA}}
\end{pmatrix}
$$

$$\hat{A}_i \hat{X}_{i-1} + \hat{B}_i \hat{X}_i + \hat{C}_i \hat{X}_{i+1} = \hat{D}_i$$

Figure 6. Same as Fig. 5, but for non-isothermal layers, where both the Planck function and its gradient are computed within each atmospheric layer.

for $\hat{X}$ involves inverting a tridiagonal matrix where the elements are the sub-matrices $\hat{A}$, $\hat{B}$, and $\hat{C}$, which may be accomplished using Thomas's algorithm (e.g. chapter 6.3 of Mihalas 1978), which first computes

$$
\hat{C}_i' = \begin{cases} \hat{C}_0 / \hat{B}_0, & i = 0, \\ \hat{C}_i / \left(\hat{B}_i - \hat{A}_i \hat{C}_{i-1}'\right), & \text{otherwise,} \end{cases} \tag{13}
$$

$$
\hat{D}_i' = \begin{cases} \hat{D}_0 / \hat{B}_0, & i = 0, \\ \left(\hat{D}_i - \hat{A}_i \hat{D}_{i-1}'\right) / \left(\hat{B}_i - \hat{A}_i \hat{C}_{i-1}'\right), & \text{otherwise,} \end{cases} \tag{14}
$$

followed by performing back-substitution,

$$
\hat{X}_i = \begin{cases} \hat{D}_{N-1}', & i = N - 1, \\ \hat{D}_i' - \hat{C}_i' \hat{X}_{i+1}, & \text{otherwise.} \end{cases} \tag{15}
$$

For non-isothermal atmospheric layers, the elements of the matrices are different, but the procedure is conceptually identical (Fig. 6).

During each iteration with `THOR` (Fig. 1), `HELIOS` uses this procedure to implement multiple scattering of radiation throughout the model atmosphere.

2.2.3 Single-scattering albedo and scattering asymmetry factor

Generally, radiation is scattered by both atoms/molecules and aerosols/condensates. For the scattering cross-section ($\sigma_{\mathrm{scat,\,gas}}$) associated with the gas, we consider Rayleigh scattering by CO_2, CO, H_2O, H, H_2, and He (Appendix C). For gas absorption,

we use the `HELIOS-K` calculator to compute molecular opacities (Section 2.1.3), which are then combined into a total absorption opacity (cross-section per unit mass),

$$
\kappa = \sum_i \kappa_i \frac{X_i m_i}{\bar{m}}, \tag{16}
$$

where the sum is over all of the molecules considered, κ_i is the opacity of the i-th molecule, X_i is its volume mixing ratio, m_i is its mass and $\bar{m}$ is the mean molecular mass of the gas. Fig. 7 shows examples of the combined opacity function. Fig. 8 shows that $\bar{m} = 2.34$ atomic mass units (amu) is a good approximation for most of the temperatures and pressures simulated by the GCM, which assumes $c_P \propto 1/\bar{m}$ to be constant.

For the absorption ($\sigma_{\mathrm{abs,\,cloud}}$) and scattering ($\sigma_{\mathrm{scat,\,cloud}}$) cross-sections, as well as the scattering asymmetry factor ($g_{0,\,\mathrm{cloud}}$), associated with aerosols/condensates, we use `LX-MIE` (Section 2.1.4) to compute them for enstatite particles assuming a monodisperse size distribution with a radius of 1 μm (Fig. 9).

The total single-scattering albedo, including gas and condensates, is constructed by weighing the terms by their respective number densities,

$$
\omega_0 = \frac{\sigma_{\mathrm{scat,gas}} + f_{\mathrm{cloud}} \sigma_{\mathrm{scat,cloud}}}{\sigma_{\mathrm{scat,gas}} + \kappa \bar{m} + f_{\mathrm{cloud}} \left(\sigma_{\mathrm{abs,cloud}} + \sigma_{\mathrm{scat,cloud}}\right)}. \tag{17}
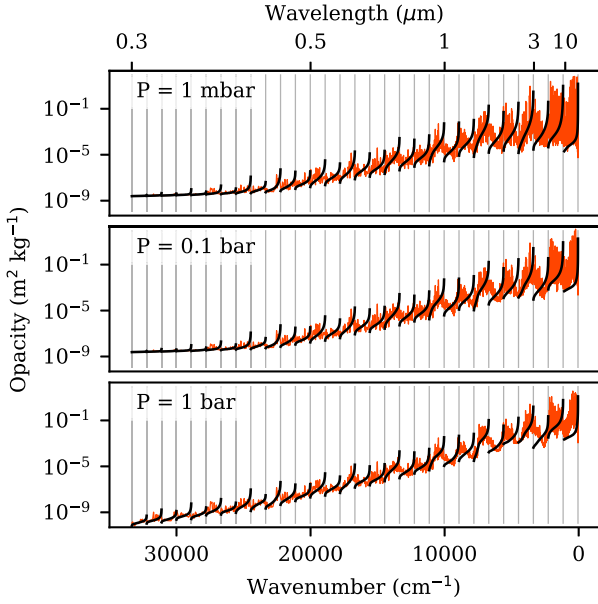$$

Similarly, the scattering asymmetry factor is

Figure 7. Examples of combined opacity function, where individual molecular opacities of H_2O, CO, CO_2, CH_4, NH_3, HCN, C_2H_2, PH_3, and H_2S are weighted by their volume mixing ratios computed assuming chemical equilibrium. Each panel represents a different pressure at a temperature of 1500 K. The Rayleigh scattering cross-sections enter into two-stream radiative transfer via the single-scattering albedo and the total optical depth. The orange curves are the high-resolution ($R = 500$; 3255 wavelength points) opacity data that is used only for post-processing. Black curves represent the k-distribution tables (30 bins with 20 Gaussian points each) that are used during integration. Vertical grey lines delineate the k-table bins.
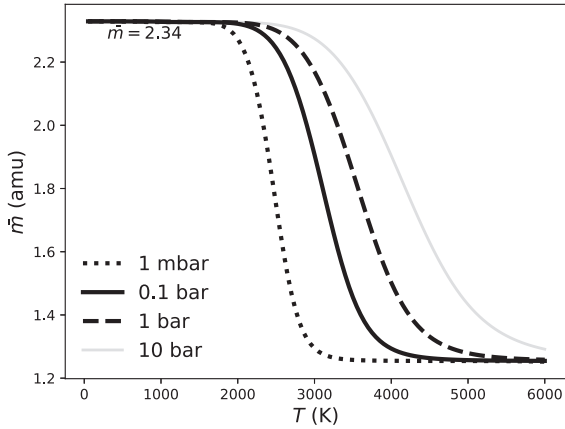

Figure 8. Mean molecular mass as a function of temperature and pressure corresponding to the equilibrium chemistry model used in the current study. At temperatures below 2000 K, the assumption of a constant mean molecular mass of $\bar{m} = 2.34$ amu, corresponding to a gas dominated by molecular hydrogen, is reasonable.

$$g_0 = \frac{f_{\text{cloud}}\sigma_{\text{scat,cloud}}}{\sigma_{\text{scat,gas}} + f_{\text{cloud}}\sigma_{\text{scat,cloud}}} \, g_{0,\text{cloud}}. \tag{18}$$

Since atoms/molecules have sizes that are much smaller than the optical/visible and infrared wavelengths considered, their scattering asymmetry factors are taken to be zero.
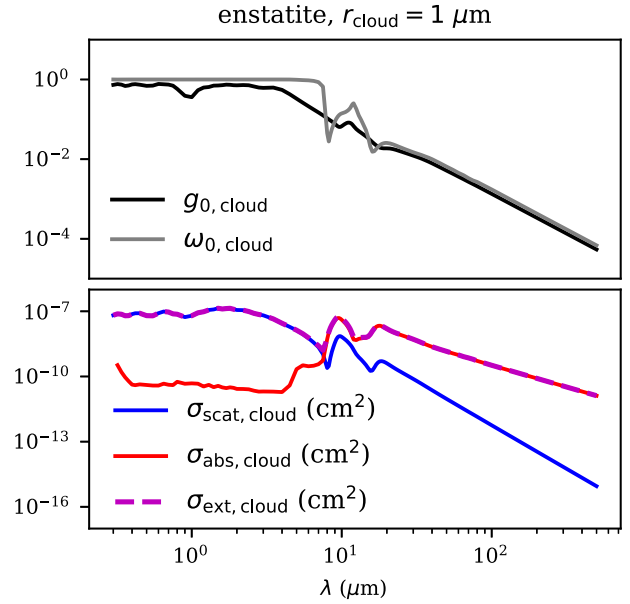

Figure 9. Absorption cross-section (σ_{abs}), scattering cross-section (σ_{scat}), total extinction cross-section (σ_{ext}), single scattering albedo (ω_0), and scattering asymmetry factor (g_0) of spherical enstatite particles. These follow a monodisperse size distribution with a radius of $r_{\text{cloud}} = 1$ μm. For the current work, we assume these quantities are independent of temperature and pressure.

The factor f_{cloud} is the ratio of number densities of the cloud to the gas. In general, it is a function of temperature and pressure, and varies throughout the model atmosphere. In the current study, we assume that f_{cloud} is a constant specified as a free parameter, i.e. a cloud-to-gas ratio by number. We use a constant value, $f_{\text{cloud}} = 10^{-17}$. The spatial homogeneity of condensates and the value chosen for f_{cloud} are not meant to correspond to a physically realistic scenario; rather, we are merely choosing this set up to test the code by making scattering and absorption by condensates easily discernible.

When k-ables are used during integration, the cloud properties and the gas scattering cross-section used in equations (17) and (18) are averaged over each k-table bin.

2.2.4 Transition between regular and improved two-stream radiative transfer methods

In the limit of an opaque ($\mathcal{T} = 0$), purely absorbing ($\omega_0 = 0$), isothermal atmospheric layer, the incoming/outgoing flux becomes ΠB, where B is the Planck function. The coupling coefficients become $\zeta_+ = 1$ and $\zeta_- = 0$, independent of the value of g_0. However, one obtains $\Pi = \pi/E$. In this limit, one should recover $E = 1$; note that, in the two-stream approach, an atmosphere with $g_0 = 1$ behaves like a purely absorbing one (Heng et al. 2014). Therefore, we expect $E \to 1$ and $g_0 \to 1$ as $\omega_0 \to 0$. Equation (31) of Heng et al. (2018) is consistent with this asymptotic limit (and was calibrated on calculations with $\omega_0 > 0.0025$), but there is no theory on how to approach it. In the absence of such a theory, we generalize equation (31) of Heng et al. (2018) to

$$E = \begin{cases} 1.225 - 0.1582g_0 - 0.1777\omega_0 - 0.07465g_0^2 & \omega_0 > 0.1, \\ \quad + 0.2351\omega_0 g_0 - 0.05582\omega_0^2, & \\ 1, & \omega_0 \le 0.1. \end{cases} \tag{19}$$

The improved two-stream approach is switched off when $\omega_0 \leq 0.1$ as it produces similar outcomes to the regular two-stream approach when $\omega_0 = 0.1$ (Heng & Kitzmann 2017). This procedure ensures that πB (with the appropriate correction term for non-isothermal layers) of flux is emitted by each atmospheric layer when it becomes opaque and purely absorbing.

2.2.5 *Operational procedure*

For each `THOR` $+$ `HELIOS` GCM run, we execute the following:

(i) Each simulation is initialized with a temperature structure given by Guillot profiles. Specifically, we use equation (27) of Guillot (2010) with the added collision-induced absorption approximation of Heng et al. (2011b), and $T_{irr} = 2440$ K, $\mu_\star = 0.5$, $\gamma = 0.5$, and $T_{int} = 100$ K. The high irradiation temperature, T_{irr}, is chosen to produce a temperature in the deep region of ~ 2200 K, which starts the model closer to radiative equilibrium.

(ii) Each GCM run is performed for 3000 Earth days (with each day having 86 400 s), which corresponds to 864 000 time-steps. A constant time step of 300 s is used. Monitoring of the global quantities suggests that dynamical equilibrium is attained only after about 1000 d (see Appendix D). We discard output from the first 2000 d and base our analysis only on output from between Days 2001 to 3000. Note that radiative equilibrium is achieved only for the cloud-free simulation (lower left panel of Fig. B1). The deep regions are still slowly adjusting at 3000 d in the cloudy cases, though the non-isothermal simulations are converging faster than the isothermal, similar to the convergence issues noted in Malik et al. (2017) for the 1D model. Nevertheless, in all simulations, the flow and temperatures do not change noticeably after ~ 1000 d.

(iii) After 3000 d, the GCM is run for one more time-step but using the high-resolution opacity file (Fig. 7), which has a spectral resolution of 500. This is a post-processing step to generate synthetic spectra of a higher resolution. For post-processing, we extend the top altitude of the simulation, extrapolating the temperatures down to pressures of ≤ 1 µbar. As only the radiative-transfer is run during this step, the instability in the dynamical core is avoided (see Section 4.3). We assume that the temperatures of each column are isothermal above the original model top and take on the value of the top-most layer. This extrapolation is used in all spectra presented in Section 4.4 and is included as an input option of our post-processing code. Users of the code can specify the desired lowest pressure level of the extrapolation.

For each simulation, we checked that the stellar beam is attenuated well before the bottom of the simulation domain (Fig. 10). If insufficient opacity is assumed in the visible/optical range of wavelengths, it is possible for starlight to pass through the entire model atmosphere, hit the bottom of the simulation domain, be artificially reflected upwards and emerge as the synthetic spectrum (not shown).

All simulations include 4th-order horizontal hyperdiffusion and 3D divergence damping. The dimensionless diffusion coefficients are $D_{hyp} = D_{div} = 0.015$ (see equation 49 of Mendonça et al. 2016 and equations 59 and 60 of Deitrick et al. 2020). We further include a 6th-order vertical hyperdiffusion term (see Tomita & Satoh 2004), with a coefficient $D_{ver} = 0.003\,75$, which helps reduce noise at the vertical grid level. In order to approximate the breaking of waves in the upper atmosphere and prevent spurious wave reflection, we include a sponge layer in the form of Rayleigh drag (Mendonça et al. 2018b; Deitrick et al. 2020) in the top 25 per cent of the model domain. Winds and temperatures are damped towards the zonal mean
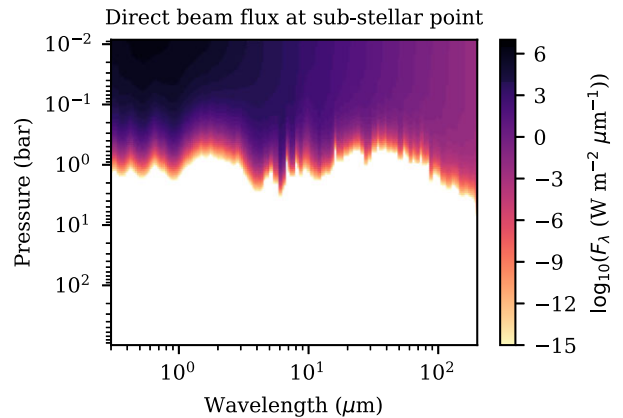

Figure 10. Flux of the direct stellar beam as a function of both wavelength and pressure. For illustration, we show calculations from the GCM of WASP-43b with non-isothermal layers and improved two-stream radiative transfer, but checked that the qualitative behaviour is similar for the other three GCMs (not shown). Fluxes below 10^{-15} W m^{-2} µm^{-1} are assumed to be zero in this plot.

in this region with a minimum time-scale of 1000 s. The strength of the sponge is gradually increased from zero at 75 per cent of the top boundary to full strength at the very top.

2.2.6 `HELIOS` *integration and code optimization highlights*

A major design bottleneck was how to interface `THOR` and `HELIOS`, especially since they are largely written in different programming languages. As already mentioned, we rewrote `HELIOS` in the C++ programming language (named `Alfrodull` for book-keeping reasons) in order to optimize the interfacing with `THOR`. Most of the computational cost associated with `HELIOS` is in solving for radiative-convective equilibrium via iteration (Malik et al. 2017, 2019). Since `THOR` has its own representation of circulation, including convection (Mendonça et al. 2016, 2018b; Deitrick et al. 2020), this feature of `HELIOS` is superfluous. There is also no requirement to solve for radiative equilibrium in one dimension, since a more general equilibrium in three dimensions is being solved for via the coupled fluid equations (see Appendix A or, e.g. chapter 9 of Heng 2017). In `THOR` $+$ `HELIOS`, the main task of `Alfrodull` is to transform abundance-weighted, temperature- and pressure-dependent opacities into fluxes, which are then integrated over wavelength to obtain heating and cooling rates.

Firstly, the workflow management of `HELIOS` was translated to C++. The code was embedded within a small library that could be used within `Alfrodull`. It was verified that the C++ translation reproduced the initial algorithm. Secondly, `Alfrodull` was interfaced as a physics module to the `THOR` code, which allowed the former to use the data storage infrastructure of the latter and to access its data. The data from the vertical spatial grid of `THOR` are converted to the pressure grid of `Alfrodull`.

Thirdly, we replace the iterative approach used in `HELIOS` (Malik et al. 2017, 2019) with the implementation of Thomas's algorithm as described in Section 2.2.2. This upgrade was motivated by tests suggesting that the implementation of an iterative, pair-wise approach over all of the columns of `THOR` in three dimensions is computationally prohibitive in practice, as each time-step took several minutes to complete. Thomas's algorithm requires one downward pass to compute the coefficients and one upward pass of back-substitution.
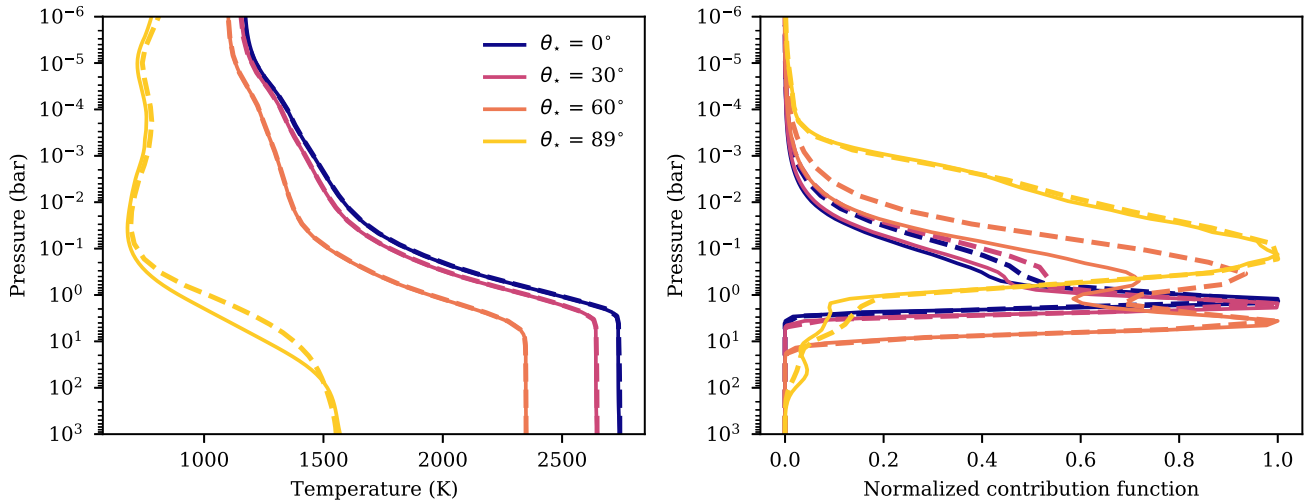
Figure 11. *Left:* Comparing THOR + HELIOS in 1D mode against 1D HELIOS, for 4 different zenith angles (θ_{star}). The solid curves are from 1D HELIOS, the dashed from THOR + HELIOS. *Right:* the thermal contribution function (normalized to its peak value) from 1D HELIOS (solid) and THOR + HELIOS in 1D mode (dashed).

This is roughly equivalent to the iterative approach taking one upward and one downward pass, which implies a gain in computational speed of a factor of roughly $\mathcal{N}$. We optimized the algorithm to run in parallel over multiple columns, provided sufficient GPU cores and memory were available. In practice, successive batches of columns are computed in serial due to memory constraints; within each batch, the columns are computed in parallel.

3 BENCHMARKING AGAINST 1D HELIOS

Here, we run several tests to validate the THOR-coupled radiative transfer by comparing to the standalone 1D HELIOS code (Malik et al. 2017, 2019). For this, we run THOR + HELIOS in '1D mode' by switching off the dynamical core and reducing the grid to a single column. The only physical processes acting on the column are the radiative-transfer followed by an adjustment to the pressure and density in each layer to preserve hydrostatic balance. Note that when the dynamical core is enabled, hydrostatic balance is continually sought by the algorithm solving the Euler equations; without the dynamical core, and because THOR utilizes an altitude grid rather than pressure, another mechanism must be enabled to retain hydrostatic balance. This extra step is unnecessary in models that utilize a pressure grid, such as 1D HELIOS, because hydrostatic balance is usually implicit in the equations.

More concretely, hydrostatic balance is enforced by the following algorithm. After the radiative-transfer module has computed the temperature of each layer, we compute the pressure. The pressure in the lowest layer is held at the reference pressure, P_{ref}. The pressure in each layer, i, above is set based on the layer below, $i - 1$, according to

$$P_i = P_{i-1} \frac{\frac{1}{z_i - z_{i-1}} - \frac{g}{2 R_d T_{i-1}}}{\frac{1}{z_i - z_{i-1}} - \frac{g}{2 R_d T_i}}, \qquad (20)$$

which is derived from the discrete equation for hydrostatic balance and the ideal gas law. After determining the pressure in each layer, the density is calculated from the ideal gas law. This does not conserve mass as the dynamical core does, but here we are only interested in reaching radiative equilibrium.

We run THOR + HELIOS in this way with four different zenith angles assigned to the direct beam: $\theta_{\star} = 0°$, $30°$, $60°$, and $89°$. Each case is run for a total of 800 d, which is more than enough to reach a steady state. We then compare to 1D HELIOS run under identical conditions. The resulting temperature–pressure profiles are plotted in the left-hand panel of Fig. 11. For all $\theta_{\star}$ except $89°$, the profiles are nearly identical. For $\theta_{\circ} = 89°$, there are minor differences but the models still match reasonably well.

We summarize the differences between the two models (1D HELIOS and THOR + HELIOS run in 1D mode) here:

(i) 1D HELIOS utilizes a pressure coordinate, while THOR + HELIOS uses an altitude coordinate.

(ii) Hydrostatic equilibrium is implicit in the use of pressure in the equations in HELIOS, though the assumption is relevant only for the calculation of layer heights. In THOR + HELIOS, hydrostatic equilibrium is not assumed in the radiative transfer equations, and therefore we adjust the density at the end of each step to restore balance.

(iii) The number of layers is 105 in HELIOS and 40 in THOR + HELIOS. The number of layers in the latter is chosen to be the same as in the full 3D simulations.

(iv) THOR + HELIOS uses a real heat capacity and a physical time-step, while in HELIOS the heat capacity is ignored and the time-step adjusts based on the heating rates.

(v) HELIOS runs until radiative equilibrium is achieved, i.e. until the upward and downward fluxes (or equivalently, the net fluxes) at each layer interface approach a constant value within some tolerance. THOR + HELIOS does not check for radiative-equilibrium and so we simply run this model until we observe a steady state.

Fig. 11 also shows the contribution function calculated from 1D HELIOS. In THOR hot Jupiter simulations, because of the altitude coordinate and the strong day–night dichotomy, the pressure at the top of the model on the day-side of the planet can be 3–4 orders of magnitude higher than the pressure at the top on the night-side. In our 3D WASP-43b simulations (Section 4), we reach pressures of $\sim 10^{-3}$ bar on the day-side and $\sim 10^{-7}$ on the night-side. As we see in Section 4.3, capturing the complete contribution function is a challenge in the full 3D simulations.
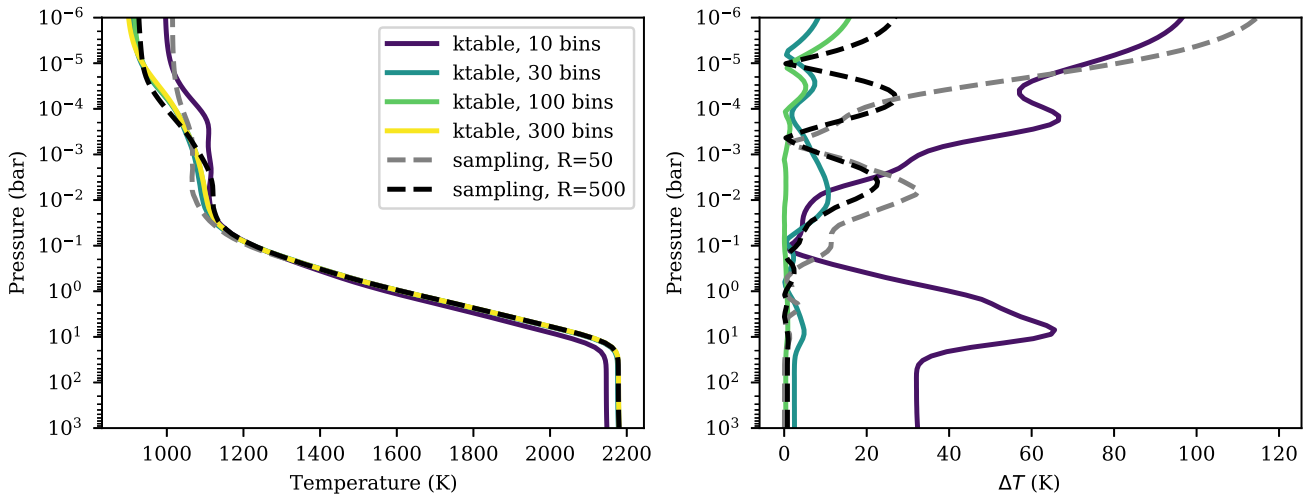
Figure 12. Comparing 1D HELIOS simulations of WASP-43b at different spectral resolutions. *Left:* Temperature–pressure profiles. *Right:* Residuals in temperature for each simulation, compared against the 300 k-table bin simulation.

To verify that our spectral resolution is sufficient, we run 1D HELIOS with several different resolutions and two different sampling methods, k-distributions and opacity sampling. The resulting temperature–pressure profiles are shown in Fig. 12. Each *T–P* profile is compared to the 300 bin k-table simulation (which contains the greatest amount of spectral information) in the right-hand panel of Fig. 12. While large errors occur for the 10 bin k-table simulation and the $R = 50$ opacity sampling solution, the others compare very well. We run our 3D simulations with the 30 bin k-table, as this provides the optimal balance between computational efficiency and numerical accuracy. With current GPUs and under our current set-up, running 3D simulations with 100 or 300 bin k-tables is computationally unfeasible. Additionally, opacity sampling at $R = 50$ is nearly as computationally expensive as using 30 k-table bins, and less spectral information is resolved. Future model design improvements, such as expanding the code to multiple GPUs, should make it possible to integrate with higher spectral resolution.

4 FOUR GCMS OF WASP-43B

To showcase the technical developments made, we construct four GCMs of the hot Jupiter WASP-43b. Due to its short (<24 h) orbital period, WASP-43b is one of the few exoplanets for which one may obtain multiwavelength phase curves using the Wide Field Camera 3 (WFC3) of the *Hubble Space Telescope* (*HST*) (Stevenson et al. 2014). Several previous studies have presented GCMs of WASP-43b (e.g. Kataria et al. 2015; Mendonça et al. 2018a, b). In the current study, our four GCMs of WASP-43b include:

(i) A radiative transfer model with isothermal layers (constant Planck function), while implementing the improved two-stream method, with enstatite condensates throughout the atmosphere.

(ii) Non-isothermal layers (which include the gradient of Planck function) with improved two-stream radiative transfer, with enstatite condensates throughout the atmosphere.

(iii) Non-isothermal layers with regular, hemispherical two-stream radiative transfer, with enstatite condensates throughout the atmosphere.

(iv) Non-isothemal layers with improved two-stream radiative transfer, but assuming a cloud-free atmosphere.

As already mentioned, our implementation of clouds in the first three GCMs is for the purpose of studying the effects of scattering as modelled using improved versus regular two-stream radiative transfer, rather than any attempt to be realistic about cloud physics. The consideration of isothermal layers in the first GCM is motivated by the study of Malik et al. (2017), which demonstrated that 1D radiative transfer models struggle to converge to radiative equilibrium even with 1001 isothermal layers, whereas models with 21 non-isothermal layers do attain convergence.

Table 3 contains the input parameters of the GCM for WASP-43b, which were curated from the published literature. All simulations include an internal heat flux at the bottom boundary, F_{BOA}, with an emission temperature of 100 K.

4.1 Estimates of computational speed

We provide two suites of estimates of computational speed. The first suite focuses solely on the THOR dynamical core: reproducing the Held-Suarez Earth benchmark (Held & Suarez 1994), which does not invoke multiwavelength radiative transfer. To match the original Held & Suarez (1994) study, we used a horizontal grid resolution of $g_{\text{level}} = 5$, which corresponds to about 2 deg on the sphere. We used 32 vertical levels. We ran each simulation for 300 time-steps with a time-step of 1000 s on four different types of GPUs. For the NVIDIA GeForce GTX 1080 Ti, GeForce RTX 2080 Ti, Tesla P100, and Tesla K20 GPUs, 300 time-steps took about 71, 36, 57, and 353 s, respectively, which corresponds to about 6.8, 3.5, 5.5, and 34 h for the full 1200 Earth days of the Held-Suarez benchmark. Simulations such as these require a lower degree of parallelization than multiwavelength radiative transfer simulations, where parallelization occurs across wavelength as well. The consumer GPU cards (1080 Ti and 2080 Ti) tend to offer similar or slightly better performance than the professional GPU card (P100) with similar compute capability.

The second suite of tests focuses on THOR $+$ HELIOS GCMs of WASP-43b and showcases the optimization efforts achieved in the current study to couple the dynamical core with multiwavelength radiative transfer. We again ran simulations for 300 time-steps. For these simulations, the horizontal resolution used is $g_{\text{level}} = 4$ (about 4 deg on the sphere), 40 vertical levels are used and

Table 3. List of input parameters.

Name	Symbol	Value	Purpose	Reference
Acceleration due to gravity	g	47 m s^{-2}	GCM	Gillon et al. (2012)
Radius[a]	R_p	1.036 R_J = 7.41 × 10^7 m	GCM	Gillon et al. (2012)
Reference pressure[a]	$P_{\rm ref}$	1 × 10^8 Pa = 1000 bar	GCM	–
Altitude at top of simulation domain	–	1.7 × 10^6 m	GCM	–
Angular rotational frequency	Ω	8.94 × 10^{-5} s^{-1}	GCM	Gillon et al. (2012)
Specific gas constant	$\mathcal{R}$	3553 J kg^{-1} K^{-1}	GCM	–[b]
Specific heat capacity	c_P	12436 J kg^{-1} K^{-1}	GCM	–[b]
Initialisation temperature	$T_{\rm eq} = T_{\rm irr}/\sqrt{2}$	1725 K	GCM	Gillon et al. (2012)
Cloud-to-gas ratio (by number)	$f_{\rm cloud}$	10^{-17}	RT	–
Semimajor axis	a	0.01525 au = 2.28 × 10^9 m	RT	Gillon et al. (2012)
Stellar radius	$R_\star$	0.667 R$_\odot$ = 4.64 × 10^8 m	RT	Gillon et al. (2012)
Stellar effective temperature	$T_\star$	4798 K	RT, stellar template	Sousa et al. (2018)
Stellar gravity	log $g_\star$	4.55 (cgs units)	Stellar template	Sousa et al. (2018)
Stellar metallicity	[Fe/H]	−0.13	Stellar template	Sousa et al. (2018)
Alpha element enhancement	[α/M]	0 (solar value)	Stellar template	–
Direct stellar beam Eddington coefficient	ϵ_2	2/3	RT	Heng et al. (2018)

[a]At bottom of simulation domain.

[b]Based on assuming 5 degrees of freedom (diatomic gas without vibrational modes activated) and $\bar{m} = 2.34$.

Note: GCM refers to the dynamical core, RT stands for 'radiative transfer'.

the time-step is about 300 s. We use the non-isothermal layer solution. Multiwavelength radiative transfer makes these simulations significantly more computationally expensive. For the 1080 Ti, 2080 Ti, P100, and K20 GPUs, 300 time-steps took about 778, 623, 580, and 1366 s, respectively, which by extrapolation correspond to about 26, 21, 19, and 46 d for our full 3000-d simulations. The professional P100 GPU card edges out the consumer GPU cards with similar compute capabilities (the 1080 Ti and 2080 Ti).

To compare more directly with the THOR + HELIOS simulations, we also ran the Held-Suarez benchmark at the same resolution ($g_{\rm level} = 4$) and number of vertical levels (40) for 1200 steps. For the 1080 Ti, 2080 Ti, P100, and K20 GPUs, these took 70, 47, 63, and 365 s, respectively. Since the two types of simulations (Held-Suarez benchmark and WASP-43b) require different time-step sizes, we can compare the time required for a fixed number of time-steps, which will give an estimate of the additional time required by the coupling to HELIOS. To run 10^6 time-steps, the Held-Suarez benchmark takes roughly 16, 11, 14.5, and 84.5 h on the 1080 Ti, 2080 Ti, P100, and K20 GPUs, respectively. The THOR + HELIOS simulations take about 720, 577, 537, and 1265 h to do 10^6 time-steps on the same GPUs. The 2080 Ti has more GPU cores than the P100, but the P100 has better double-precision compute power. However, since we do not see this benefit of the P100 in the Held-Suarez test, we may surmise that the calculation is dominated by memory access. We conclude that our implementation of HELIOS (Alfrodull) is not memory-access-limited, which enables the P100 GPU to run optimally.

4.2 Basic climatology

For the four GCM models presented in this study, the familiar chevron-shaped feature (Showman & Polvani 2011; Tsai, Dobbs-Dixon & Gu 2014) is shown in Fig. 13. The zonal-mean profiles are shown in Fig. 14 (temperature), Fig. 15 (potential temperature), Fig. 16 (zonal wind), and Fig. 17 (streamfunction). Since a non-hydrostatic GCM is being used, P is not a coordinate like in a GCM that solves the primitive equations, but rather a quantity that varies with time and location. Therefore, to produce Figs 14–17

we have computed the temporally, latitudinally (meridionally), and longitudinally (zonally) averaged pressure $\bar{P}$. The maximum value of this 1D array is $\bar{P}_{\rm max}$.

The Eulerian-mean streamfunction is defined as (Peixóto & Oort 1984; Pauluis, Czaja & Korty 2008)

$$\Psi = \frac{2\pi R_p \cos\theta}{g} \int_0^{\bar{P}} \bar{v}_\theta \, d\bar{P}, \qquad (21)$$

where θ is the latitude and $\bar{v}_\theta$ is the temporally and zonally averaged meridional velocity. The convention is chosen such that positive values of Ψ correspond to clockwise circulation (Frierson et al. 2006). Note that the preceding expression is slightly different from equation (21) of Heng et al. (2011b), who omitted the factor of 2π. The integral was computed using a trapezoidal rule (the trapz routine in PYTHON (Virtanen et al. 2020)). Fig. 17 shows the large-scale circulation cells with air *descending* at the equator at pressures above ∼0.1 bar (opposite from the case of Earth), a phenomenon that was previously elucidated by Showman & Polvani (2011), Tsai et al. (2014), Charnay, Meadows & Leconte (2015), and Mendonça (2020).

To construct Fig. 15, the zonal-mean potential temperature is defined as

$$\bar{\Theta} = \overline{T\left(\frac{P}{P_{\rm ref}}\right)^{-\kappa}}, \qquad (22)$$

where $\kappa = \mathcal{R}/c_P \approx 2/7$ is the adiabatic coefficient (Pierrehumbert 2010; Heng 2017) and $\bar{T}$ is the zonal-mean temperature.

These zonal-mean profiles are qualitatively consistent with those reported in previous studies (e.g. Showman et al. 2009; Heng et al. 2011a, b; Mayne et al. 2014a, b; Deitrick et al. 2020), showing an irradiated atmosphere that is stable against convection and possessing a super-rotating jet at the equator and large-scale circulation cells. Unsurprisingly, temperatures in the cloudfree GCM are the highest among the four (Fig. 14) as the absence of clouds means that less starlight is reflected away and more heating of the atmosphere occurs. The zonal jet in this case is faster and broader than in the cloudy cases (Fig. 16), while the meridional circulation in the deep region is stronger by roughly an order of magnitude (Fig. 17). The stronger
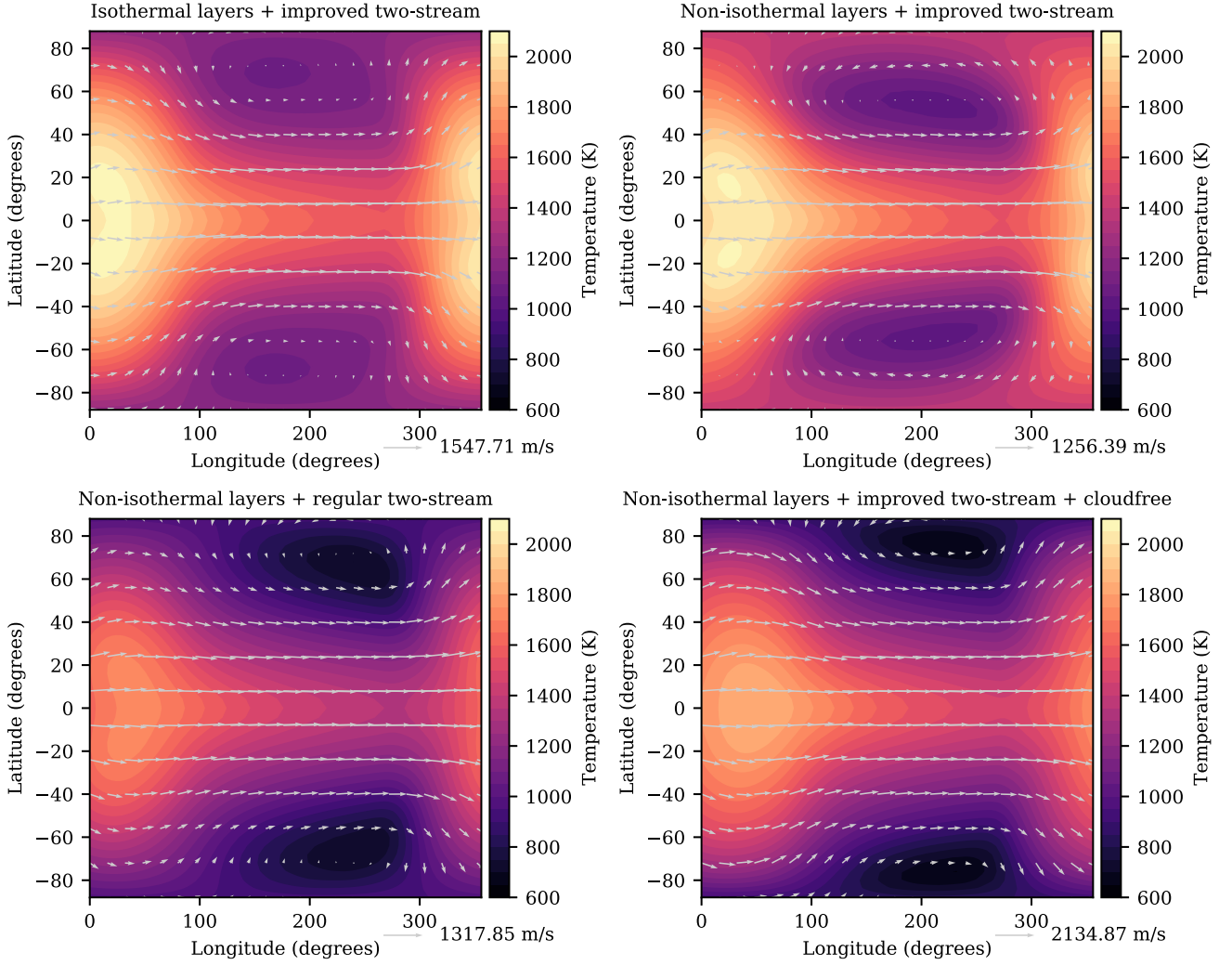
Figure 13. Temperature slice of each of the four GCMs presented in the current study, as labelled in each subpanel. The selected altitude is 1200 km from the bottom of the simulation domain, which corresponds to ~0.1 bar. The scale of wind vectors is indicated in the lower right of each panel.

heating leads to a stronger jet (higher velocities; Fig. 16) and more vigorous circulation (Fig. 17).

4.3 Comparison of radiative-transfer solutions

Figs 13–17 demonstrate that the qualitative features of the climatology are only mildly sensitive to whether regular versus improved two-stream radiative transfer – or whether isothermal versus non-isothermal layers – is employed. The same general atmospheric structure appears in all cases. Still, some differences are noteworthy. Temperatures are higher near 0.1 bar for the improved two-stream solution (see next paragraph). The improved two-stream solution also has a slower equatorial jet and weaker meridional circulation. The non-isothermal layers solutions also present retrograde flow at high latitudes, a feature that is absent from the isothermal solution in its zonal average.

Temperature–pressure profiles at various locations are plotted for all simulations in Fig. 18. Here, differences in the temperatures around ~0.1 bar are discernible for the regular and improved two-stream (right column); mainly, the regular two-stream is cooler in this region, consistent with the finding that this method overestimates

back-scattering of photons (Kitzmann et al. 2013; Heng & Kitzmann 2017).

Though the isothermal layer solution produces qualitatively similar results to the non-isothermal layer solution, we can see a large departure of the temperature in the deep region (Fig. 18). The isothermal solution is ~200 K cooler at pressures above ~10 bar. Malik et al. (2017) observed the same issue in their simulations with 1D HELIOS (see their fig. 9), noting that the isothermal layer solution requires ≳1000 vertical layers to achieve convergence, while the non-isothermal merely requires ~20. Using 1000 or more layers in THOR + HELIOS is computationally infeasible. Moreover, we find that the speed increase afforded by the isothermal solution is less than a factor of 2, compared to the non-isothermal with the same number of vertical levels. For these reasons, we strongly advise the usage of non-isothermal layers.

The temperature–pressure profiles in Fig. 18 reveal a limitation of non-hydrostatic GCMs applied to hot Jupiter forcing regimes – the pressure at the top of the model in the hottest locations is between 10^{-2} and 10^{-3} bar. This limitation occurs because the dynamical core is unstable below ~10^{-6} bar. In the present forcing regime, when the pressure at the top of the model in the coolest locations is ≲10^{-6} bar, the top boundary pressure in the hottest regions is
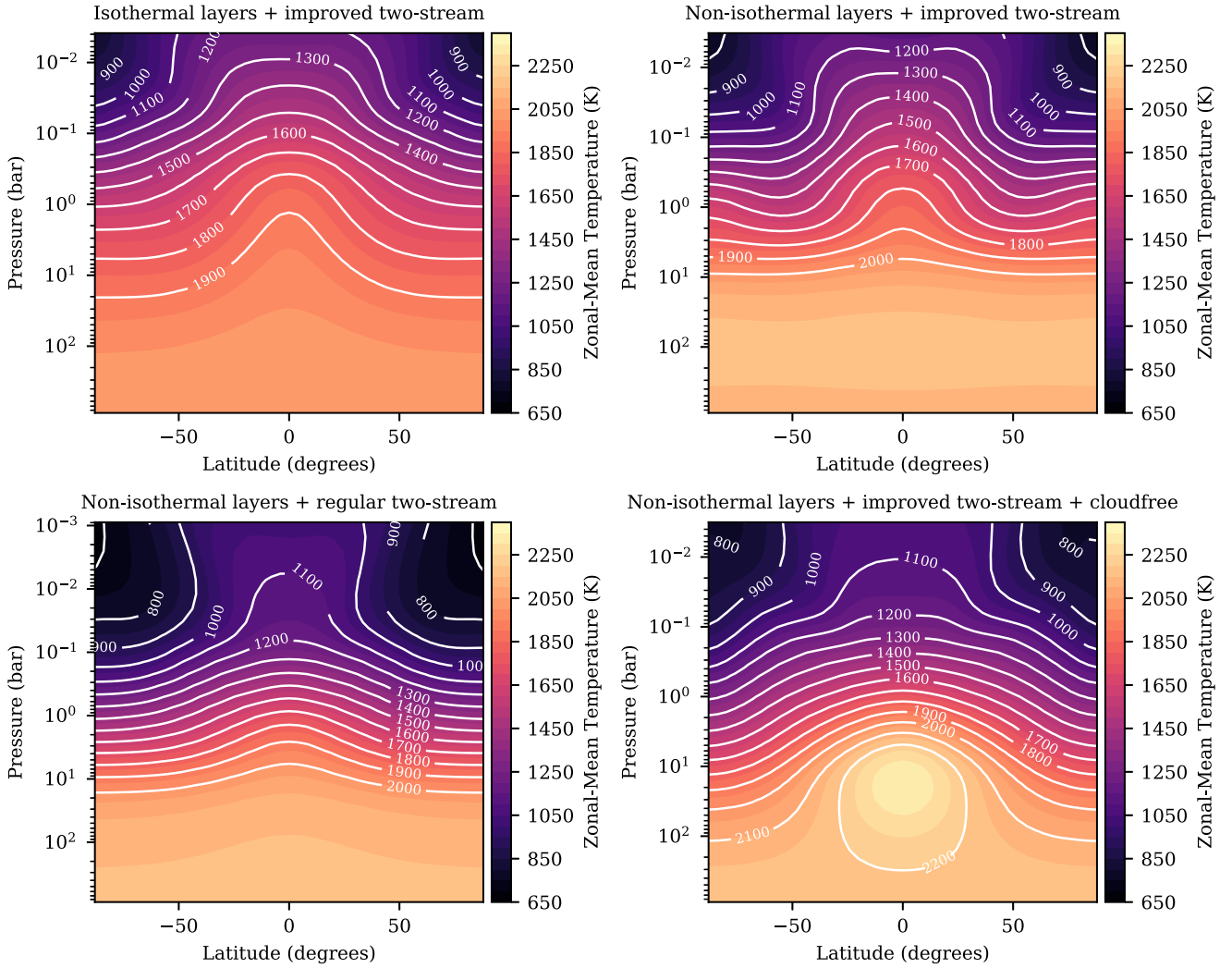
Figure 14. Zonal-mean temperature profiles of the four GCMs presented in the current study, as labelled in each subpanel.

up to 4 orders of magnitude larger. We ran a number of additional simulations that increased the height of the top boundary, but were unable to stabilize any reaching higher than the ones presented here. Note that prior THOR simulations of hot Jupiters (Mendonça et al. 2018a, b; Deitrick et al. 2020) have extended to pressures $<10^{-3}$ bar on the day-side, including for WASP-43b, when dual-band grey radiative transfer was used. The important difference is that the multiwavelength radiative transfer in this case enhances the day–night temperature difference, increasing the probability of triggering the instability.

Since our primary concern in this paper is to test the radiative transfer module, the more important question is whether or not these simulations extend high enough to capture the peak thermal emission. Fig. 19 shows the wavelength-integrated contribution function (equation 24 of Malik et al. 2019) for all 4 simulations at different locations. The peak of the contribution is captured at all locations, however, it does not reach zero before the model top at locations along the equator. This is one difficulty with our current algorithm that we have been unable to circumvent with numerical diffusion. We are exploring other solutions at present, however, these require a major reworking of the dynamical core code.

4.4 Reflected light versus thermal emission: synthetic spectra and phase curves

While there are noticeable differences in the global structure of our WASP-43b GCMs, depending on the radiative transfer solution, the output spectra are mostly indistinguishable. Fig. 20 shows the outgoing spectra at the top of the atmosphere at the sub-stellar point. Fig. 21 shows the same at the substellar longitude near the pole. Other than the cloud-free case, the only discernible differences are in the total emission between 2 and 4 μm in the polar region. As described in Section 2.2.5, we have extrapolated each column down to a pressure of ≤ 1 μbar to produce these spectra and the following phase curves.

To explore the emission further, we post-process the synthetic spectra at different orbital phases into phase curves by adapting the formalism of Cowan & Agol (2008)

$$F = \int_{\lambda_1}^{\lambda_2} \int_{\phi_1}^{\phi_2} \int_{-\pi/2}^{\pi/2} \frac{F_{\mathrm{TOA}}}{\pi} \cos^2\theta \cos(\phi - \alpha) \, \mathrm{d}\theta \, \mathrm{d}\phi \, \mathrm{d}\lambda, \qquad (23)$$

where F_{TOA} is the top of atmosphere (TOA) flux, at a given wavelength, emerging from each atmospheric column of the GCM.
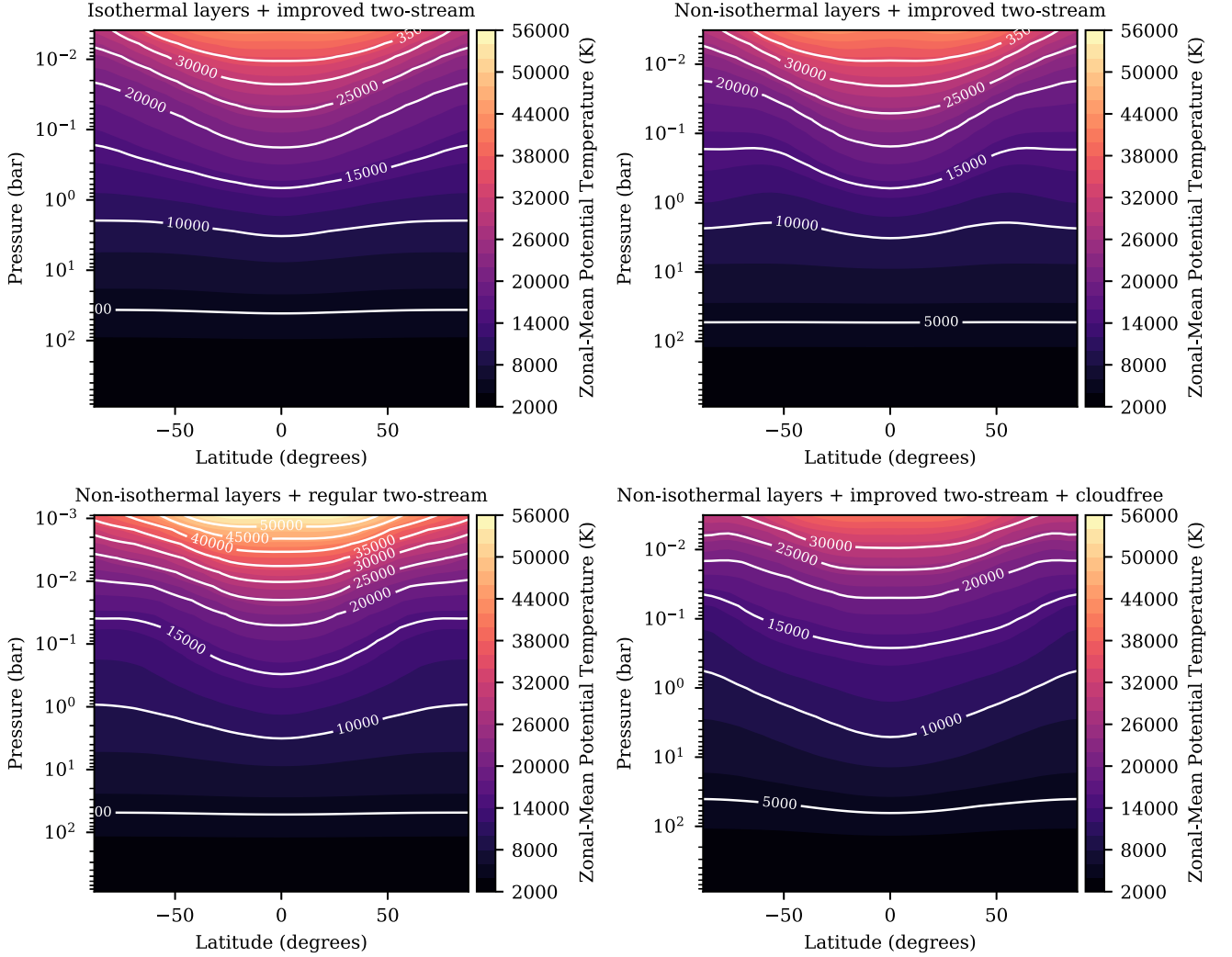
Figure 15. Zonal-mean potential-temperature profiles of the four GCMs presented in the current study, as labelled in each subpanel.

To simulate the flux measured by the HST-WFC3 instrument, we integrate F_{TOA} from $\lambda_1 = 1.1$ μm to $\lambda_2 = 1.7$ μm. Two factors of cosine account for the diminution of flux due to geometric projection across latitude and longitude; the third comes from the solid angle element, $d\Omega$. The latitude and longitude are denoted by θ and ϕ, respectively, while the orbital phase angle is denoted by α. The integration limits,

$$\phi_1 = -\alpha - \frac{\pi}{2}, \ \phi_2 = -\alpha + \frac{\pi}{2}, \tag{24}$$

associated with the longitude depend on the exact value of $-\pi \leq \alpha \leq \pi$ since the GCM adopts the convention of $0 \leq \phi \leq 2\pi$.

This integral is most easily performed on the icosahedral grid in the discrete form,

$$F = \sum_i^n \frac{F_{TOA,i}}{\pi} \mu_i \frac{A_i}{R_p^2}, \tag{25}$$

where i is the icosahedral grid index, μ_i is cosine of the angle of each location with respect to the line of sight, and A_i is the area of each control volume at the top of the atmosphere. The solid angle element $d\Omega = \cos\theta \, d\theta \, d\phi$ becomes A_i/R_p^2 in discrete form. By defining μ_i

with the conditions,

$$\mu_i = \begin{cases} \cos\theta\cos(\phi - \alpha), & \alpha - \frac{\pi}{2} < \phi < \alpha + \frac{\pi}{2}, \\ 0 & \phi > \alpha + \frac{\pi}{2} \text{ or } \phi < \alpha - \frac{\pi}{2}, \end{cases} \tag{26}$$

we can do a simple summation over the entire grid to calculate the total received flux. Essentially, this step sets all fluxes emerging from the opposing, out-of-sight hemisphere of the planet to zero.

Fig. 22 shows the HST-WFC3-like phase curves associated with the four WASP-43b GCMs. The differences between the phase curves employing isothermal versus non-isothermal layers are about 14 per cent maximum. However, the difference between the phase curves employing regular versus improved two-stream radiative transfer is about 15 per cent on average and rises to as high as 38 per cent.

When clouds are absent, reflected light is confined to visible/optical wavelengths. However, when clouds are present, reflected light at ∼1 μm and longer wavelengths becomes non-negligible (Figs 20 and 21), a fact further supported theoretical calculations of hot Jupiter albedos (see fig. 13 of Morris et al. 2021). Fig. 22 supports this conclusion, although we note that the eastward peak offset of the phase curve associated with the three cloudy GCMs is about 2° compared to the 12.3 ± 1° shift measured by Stevenson et al. (2014).
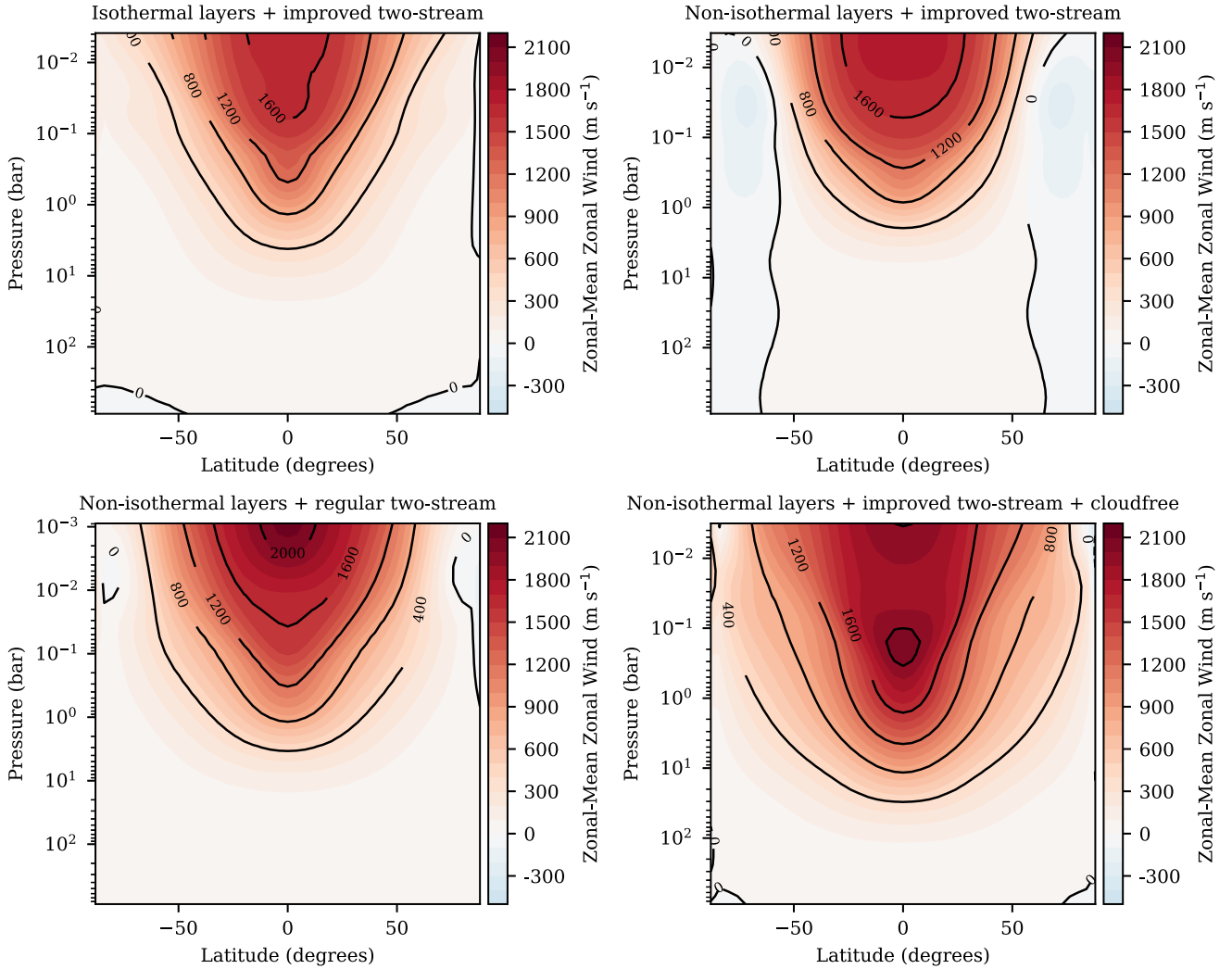
Figure 16. Zonal-mean zonal wind profiles of the four GCMs presented in the current study, as labelled in each subpanel.

The cloudfree GCM phase curve has a eastward peak offset of about 45.5°. Together, these suggest that the degree of cloudiness present in WASP-43b is non-zero, but less than what we have assumed for the three cloudy GCMs. Nevertheless, these findings suggest that more careful modelling of reflected light versus thermal emission may be required to separate the two components when decontaminating measurements of the geometric albedo via visible/optical secondary eclipse observations.

Fig. 22 also shows the spectra of day-side and night-side for each model, relative to the stellar flux. The cloudy simulations have a much larger difference in the emission between day and night at longer wavelengths than the cloud-free simulation. These simulations also do a bit better at matching the day-side *Spitzer* observations at 3.6 and 4.5 μm (Stevenson et al. 2017), though not as well as the cloud-free result from Venot et al. (2020) or the night-side cloud case from Mendonça et al. (2018a). None of the simulations match the original night-side *Spitzer* observations, though we note that Venot et al. (2020)'s model with enstatite clouds (not shown here) matches these observations well. At the same time, several models are consistent with the re-analysed night-side *Spitzer* points from Mendonça et al. (2018a). In our cloudy models, there is also a small upward tilt in the spectrum toward ∼1 μm; this is due to scattering by condensates.

In fact, it has previously been argued that some reflected light is present in the observations of this planet (Keating & Cowan 2017), though recent measurements suggest the day-side is very dark in the optical and probably cloud free (Fraine et al. 2021). The fact that we overestimate the flux at these wavelengths is another indication that the models presented here are too cloudy, particularly on the day-side. At the same time, however, it appears even our cloud-free model produces too much reflection in the optical. Future investigations should attempt to understand this discrepancy.

We also note that at longer wavelengths (2–20 μm), our cloud-free GCM produces less flux on the day-side than the similar models from Mendonça et al. (2018a) and Venot et al. (2020). At the same time, the night-side flux in this range is comparable to Venot et al. (2020) (the simulation from Mendonça et al. (2018a) is dimmer on the night-side, due to the inclusion of night-side clouds). The list of opacity sources is quite similar between the three simulations, thus the day-side flux should be closer, assuming the same temperatures. In fact, this is the key difference between the simulations – comparing to the simulation from Mendonça et al. (2018a), our cloud-free simulation is ∼500 K cooler on the day-side around pressures of 0.01 − 0.1 bar. Thus the day-side is fainter in our simulation simply because it is cooler in the photosphere. This is discussed in further detail in
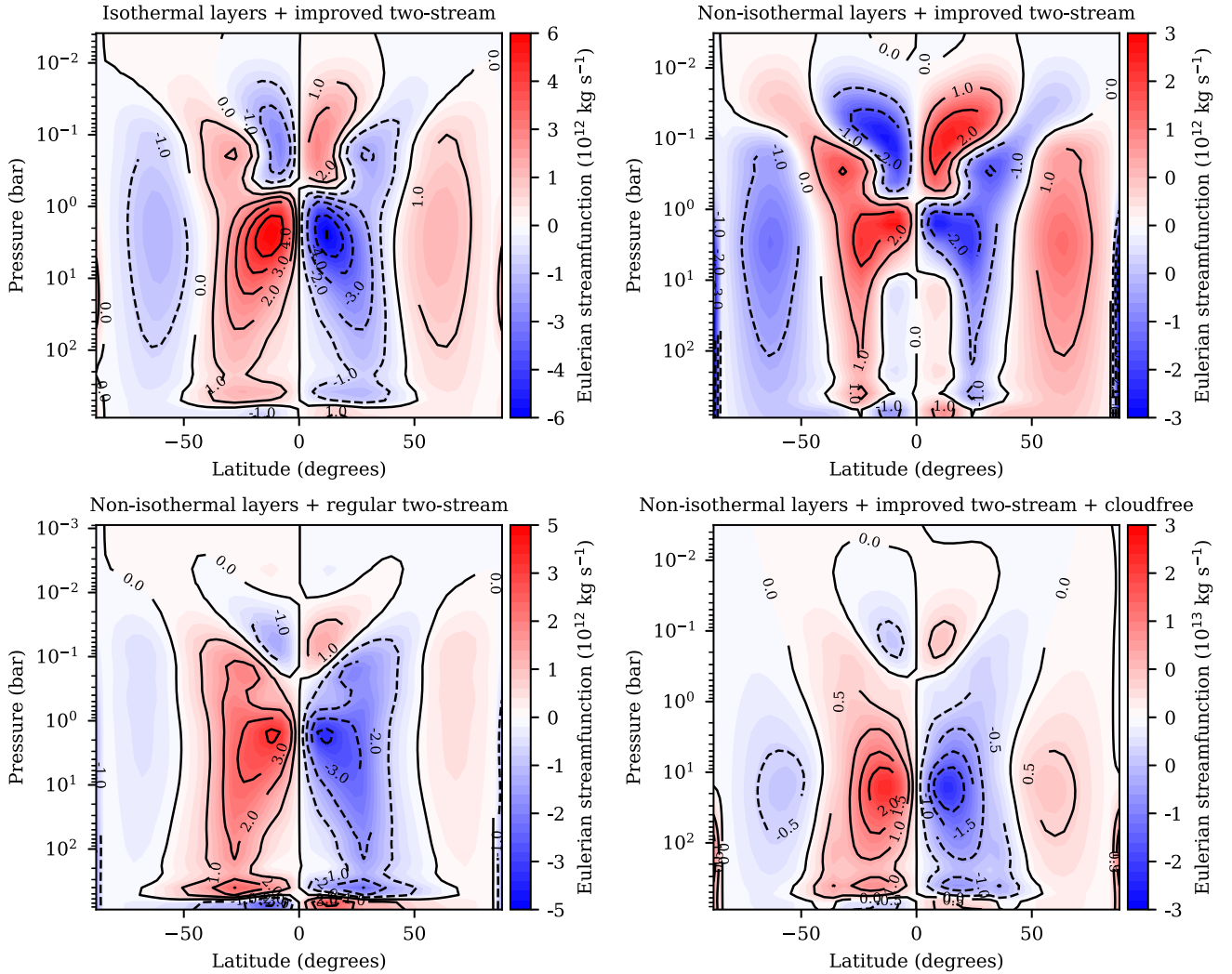
Figure 17. Eulerian-mean streamfunction profiles of the four GCMs presented in the current study, as labelled in each subpanel. Note that the scale in the lower right panel is an order of magnitude higher than the other three panels.

Appendix E. Despite the increased realism of the radiative-transfer solver in this work compared to the Mendonça et al. (2018a), the latter of which used dual-band grey radiative transfer in their GCM, the Mendonça et al. (2018a) result produces day-side temperatures that better match the *Spitzer* observations.

A potential source of the temperature discrepancy between our cloud-free simulation and that of Venot et al. (2020) is the lack of alkali species in our opacity list. This was shown to be an important source of opacity by Freedman, Marley & Lodders (2008). Especially their strong, non-Lorentzian line wings can cause significant absorption near the resonance line centers (Allard, Spiegelman & Kielkopf 2016; Allard et al. 2019). Though this work is primarily focused on detailing our new radiative transfer framework, rather than on explaining all the available data, we acknowledge the importance of species like Na and K and intend to include them in future works.

For cloud-free models, the Kataria et al. (2015) simulation is a better fit to the phase curve data than ours in terms of the amplitude and offset. Our cloudy simulations fit the amplitude better, especially regarding the extremely faint night-side. From Fig. 19 we can see that the extremely low night-side flux is a consequence of the photosphere being at much lower pressure than in the cloud-free case. However,

we see that much of the phase amplitude in these simulations is due to reflection. This and the small phase offset are further indications that we are overestimating the reflected light at short wavelengths (~1 μm). None of the simulations in this work fits the phase curve quite as well as the prior THOR simulation from Mendonça et al. (2018a). This simulation utilized dual-band grey radiative transfer – the spectral information in Fig. 22 was produced via post-processing with 1D HELIOS.

Future work with THOR will explore this issue for more realistic cloud models, as has been done recently with other GCMs (Roman & Rauscher 2017, 2019; Parmentier et al. 2018; Lines et al. 2019; Christie et al. 2021; Parmentier et al. 2021; Roman et al. 2021).

Equation (23) does not take into account limb darkening of the planet, which may be relevant for inflated or low density planets. One method to include limb darkening may be the use of an empirically tuned model such as used for stars (Sing et al. 2009, for example), applied to the thermal emission. Another method, which is more predictive, is to repeat the two-stream radiative transfer step at output with angle-averaging replaced by the viewing angle of the observer (Fortney et al. 2006). Yet another predictive method is to use a Monte Carlo radiative-transfer model for postprocessing, such as Lee
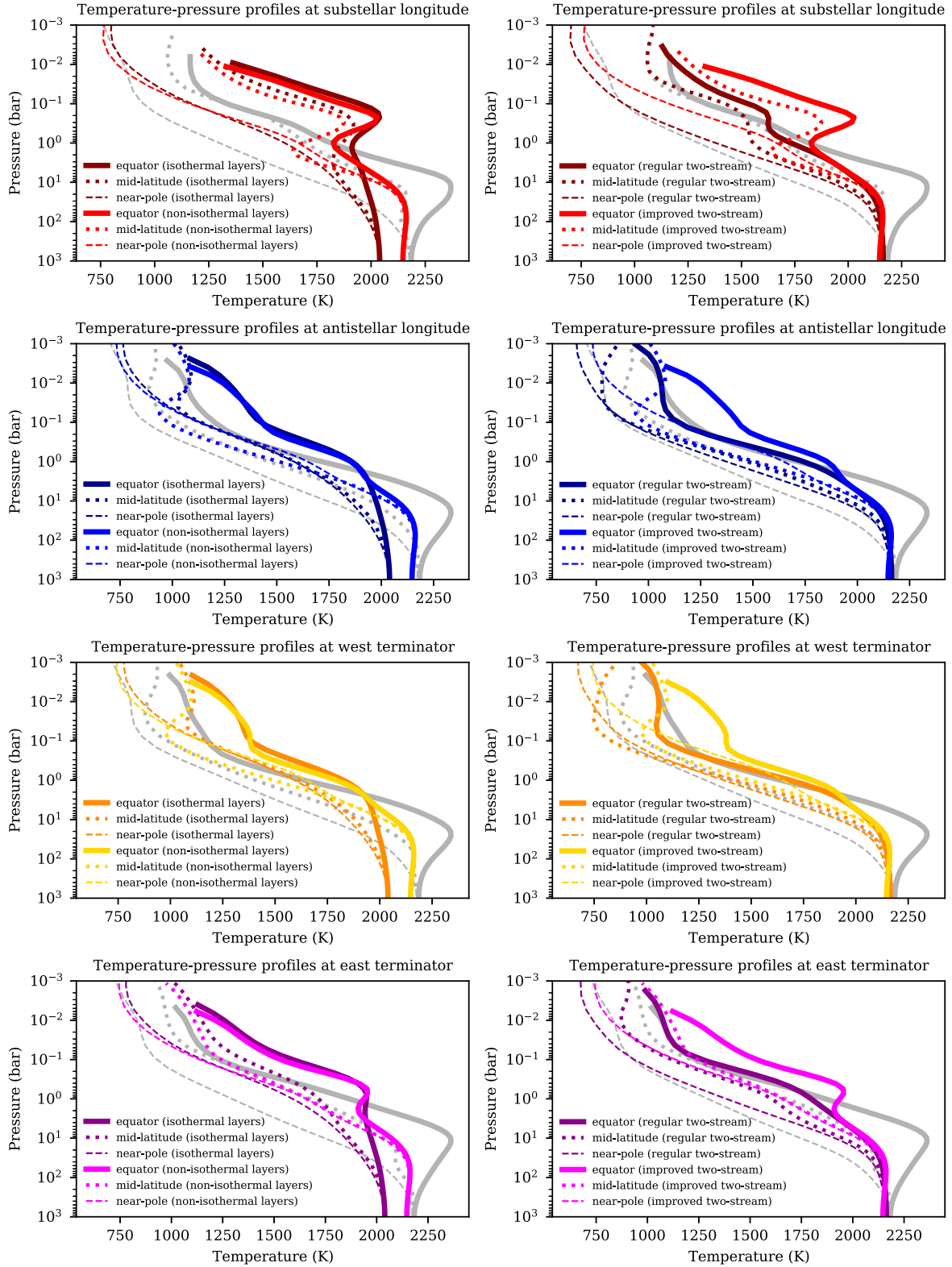
Figure 18. Temperature–pressure profiles comparing isothermal versus non-isothermal radiative transfer (left column) and regular versus improved two-stream radiative transfer (right column) at the substellar longitude (first row), antistellar longitude (second row), west terminator longitude (third row) and east terminator longitude (fourth row). For each longitude, the equator, mid-latitude and near-pole temperature profiles are shown. For each panel, the grey curves are of the cloudfree case.
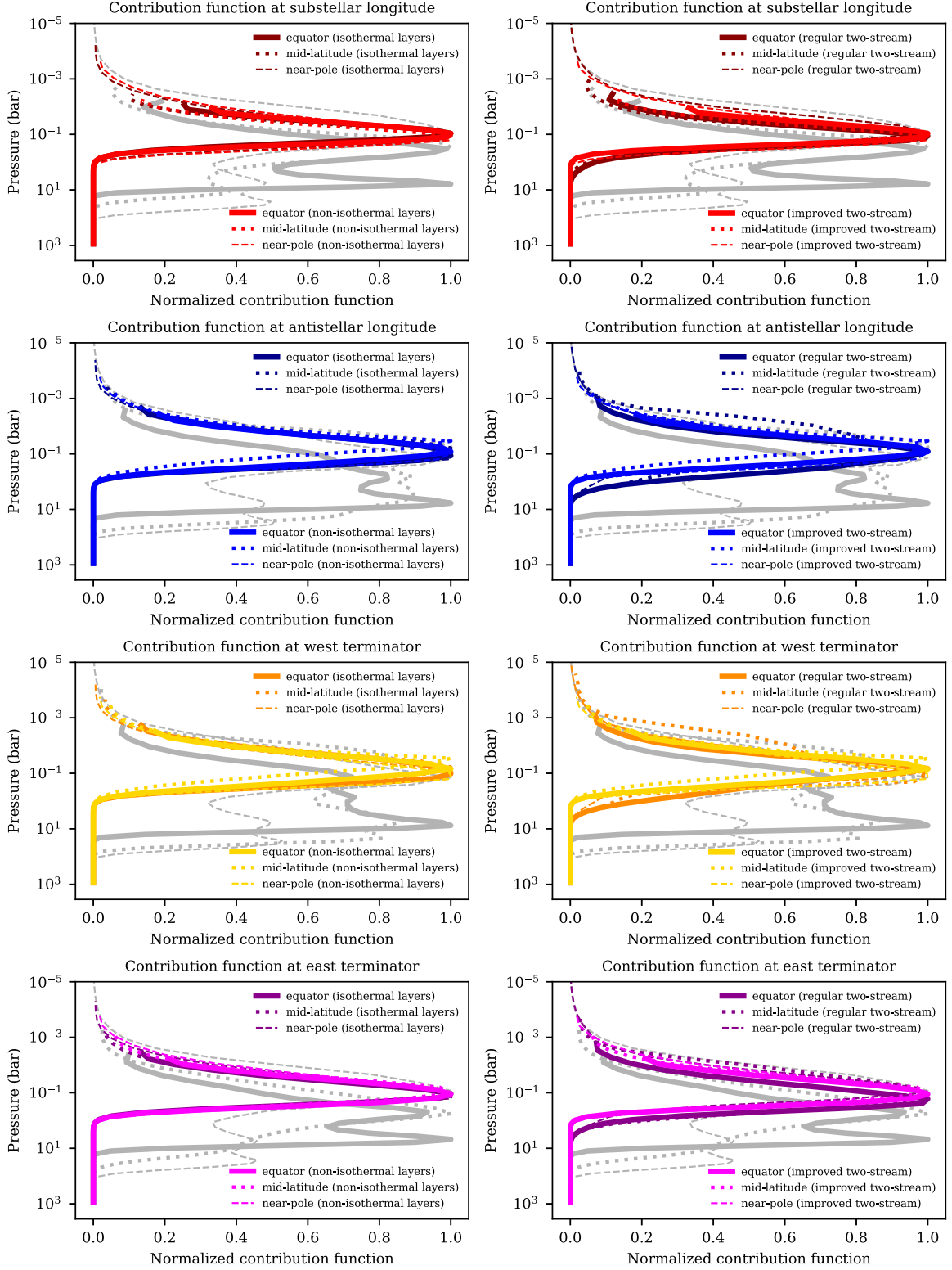
Figure 19. Wavelength-integrated contribution function as a function of pressure, comparing isothermal versus non-isothermal radiative transfer (left column) and regular versus improved two-stream radiative transfer (right column) at the substellar longitude (first row), antistellar longitude (second row), west terminator longitude (third row) and east terminator longitude (fourth row). For each longitude, the equator, mid-latitude and near-pole temperature profiles are shown. For each panel, the grey curves are of the cloudfree case. The planet's photosphere is defined by the peak of the contribution function. In the cloud-free case, there is more than one peak – an indication that there are 'spectral windows' at different wavelengths.
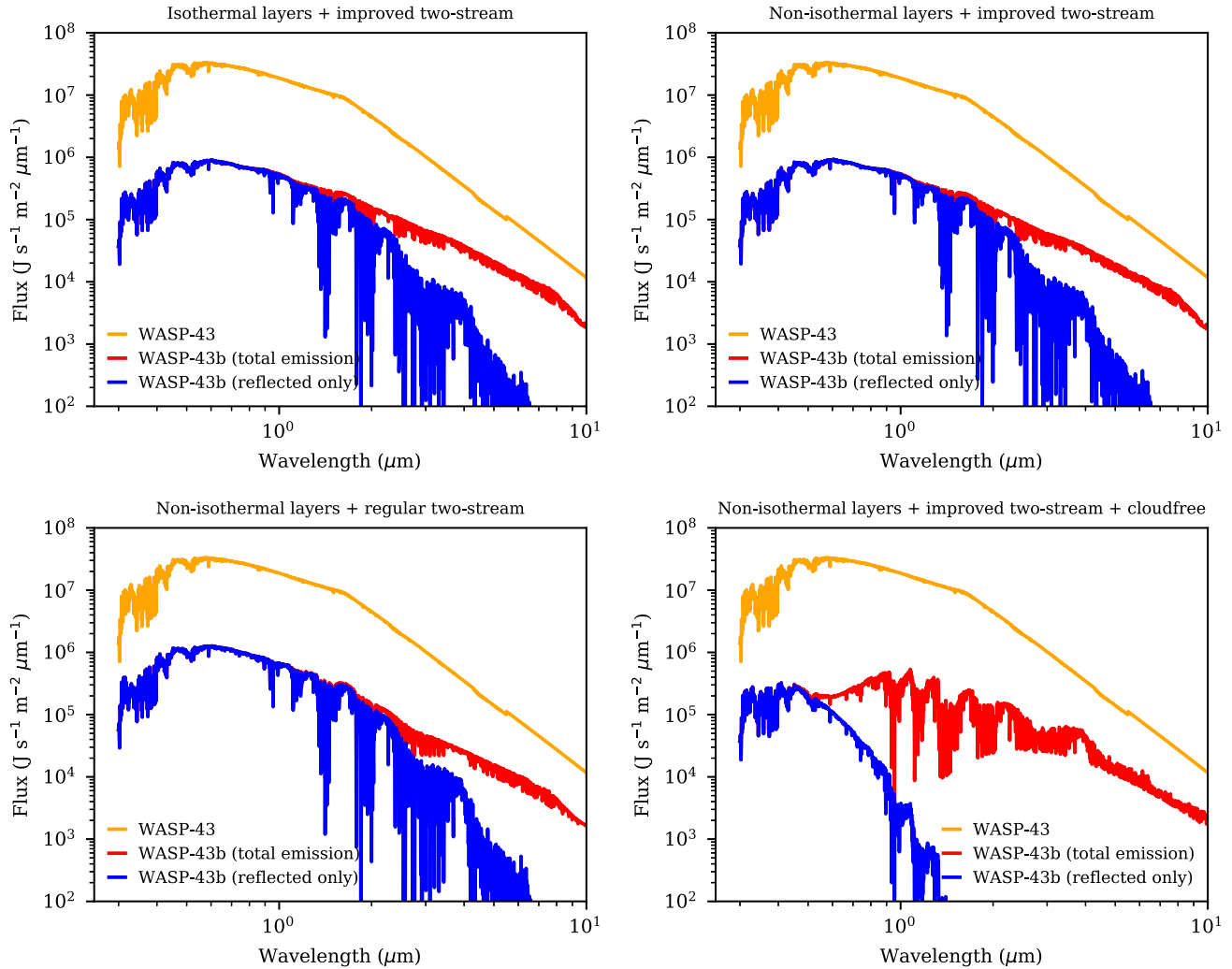
Figure 20. Comparing the synthetic spectra of our WASP-43b GCMs with the incident stellar spectrum at the substellar point. Planet spectra are post-processed at the end of each 3000 d simulation, using opacity sampling at $R = 500$.

et al. (2017, 2019), which naturally takes into account the greater path-length at the planet limb. It should be noted, however, that symmetric features do not appear in phase curves alone (Cowan & Agol 2008), though spectra may ultimately be affected by the cooler temperatures probed at the limb. Thus, unless it is strongly asymmetrical, secondary eclipse mapping (e.g. De Wit et al. 2012) may be necessary for constraining planetary limb darkening. It is beyond the scope of this paper to include the effects of limb darkening on the emission spectrum, though this is an interesting avenue for future development.

5 DISCUSSION

5.1 Summary of key developments and findings

In the current study, we report the merging of the THOR GCM and HELIOS radiative transfer solver, as well as the incorporation of improved two-stream (corrected back-scattering) radiative transfer into a GCM. Key aspects of the study include:

(i) Radiative transfer is sped up by ∼2 orders of magnitude, compared to the iterative method originally used in the

standalone HELIOS code, by implementing Thomas's algorithm to compute multiple scattering of radiation across all layers simultaneously.

(ii) Since radiative transfer is performed independently in each atmospheric column, we have invested effort into optimizing it by performing these computations in parallel on a GPU.

(iii) Using the hot Jupiter WASP-43b as a case study, we show that the global climate is qualitatively robust to whether regular versus improved two-stream radiative transfer or isothermal versus non-isothermal layers are employed, but simulations differ in the finer details. Emission spectra are nearly indistinguishable by eye, however, when integrated to produce HST-WFC3 phase curves, the differences are ∼ 10 per cent.

(iv) The crude assumption of a constant condensate abundance throughout the atmosphere overproduces reflection, as shown by the phase offset and day-side spectrum at ∼1.1 μm (Fig. 22). Nevertheless, the fact that these cloudy simulations match the phase amplitude and offset better than cloud-free simulations indicates that some amount of reflection by clouds is present in the observations. This appears to be contradicted by the extremely shallow secondary eclipse observed by Fraine et al. (2021), however, which found that
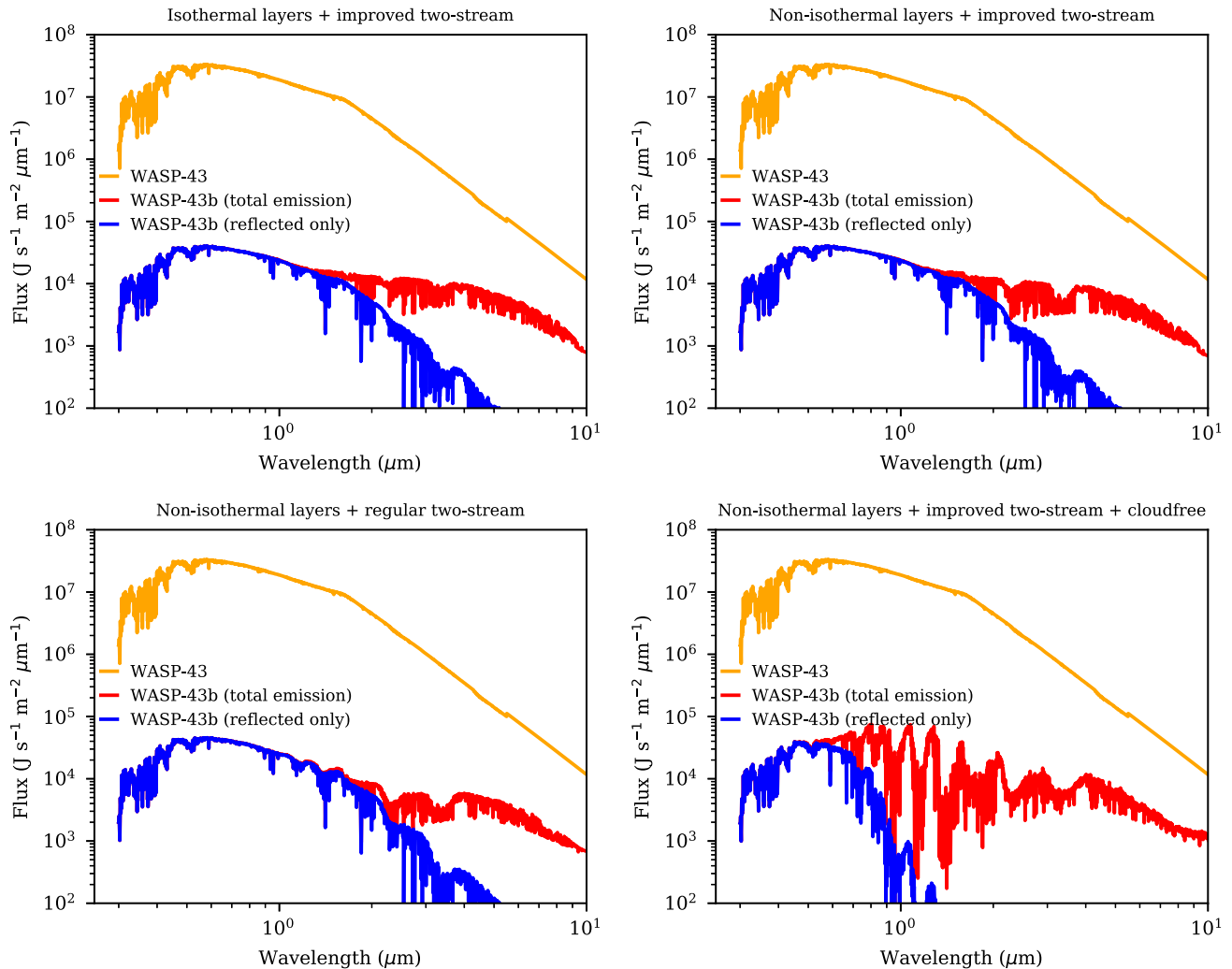
Figure 21. Same as Fig. 20, but at a latitude of 88° (near the north pole). The longitude is the same as that of the substellar point.

the day-side is very dark and, in all likelihood, cloud-free. Future investigation with a realistic assumption for cloud distribution using THOR + HELIOS should address this contradiction.

(v) A WASP-43b GCM executed for 3000 Earth days with a constant time step of 300 s approximately 19 d to complete on a Tesla P100 GPU card. The computational time taken for other GPU cards are also reported.

(vi) The results in Figs 18 and 19 highlight a challenge of non-hydrostatic modelling of hot Jupiters: instabilities at low pressure prevent us from extending the atmosphere on the day-side to completely capture all components of the radiation. Hydrostatic models, which generally utilize a pressure grid, are capable of reaching pressures of ∼1 μbar in hot regions, but will become inaccurate when the model domain is ∼ 20 per cent of the planet radius, as is the case for many smaller exoplanets (Mayne et al. 2019). We are currently exploring solutions to the low pressure instability in THOR and hope to resolve this issue in a future work. Unfortunately, the problem worsens in higher temperature regimes, due to the increasing day–night dichotomy. This prevents us from modeling ultrahot Jupiters, for example, at present. Users are advised to plot the contributions functions, as we have in Fig. 19, to verify that the bulk of the radiative energy budget is captured by the model domain.

5.2 Future work

Future work should replace the simplistic cloud model employed in the current study with a more realistic, first-principles cloud model (e.g. Lee et al. 2016, 2017), where f_{cloud} is a function of location, pressure, and temperature (Lines et al. 2019; Christie et al. 2021). Ideally, clouds can be modelled using dynamical tracers, although even a static parametrization based on local quantities would be a step beyond our crude assumption in this work. Chemical disequilibrium driven by atmospheric circulation may be modelled using the technique of chemical relaxation with passive tracers (Cooper & Showman 2006; Drummond et al. 2018; Mendonça et al. 2018b; Tsai et al. 2018). THOR + HELIOS may also be used to simulate ultra-hot Jupiters, but this requires the incorporation of a non-constant specific heat capacity as the atmosphere transitions from being dominated by atomic hydrogen on the dayside to being dominated by molecular hydrogen on the nightside (Bell & Cowan 2018; Parmentier et al. 2018; Komacek & Tan 2018; Tan & Komacek 2019). As we head into the era of JWST, THOR + HELIOS may be used to provide 'null hypothesis' models that assume the same elemental abundances as the host or parent star, where transmission spectra, emission spectra, multiwavelength phase curves and predictions on variability may be self-consistently computed and confronted by data.
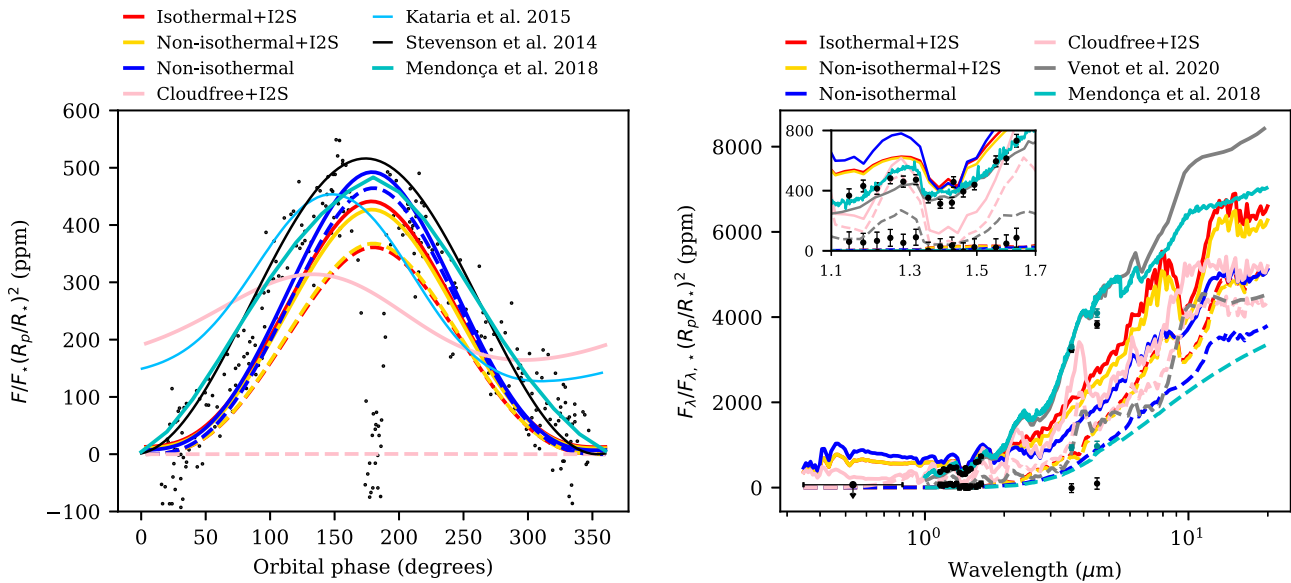
Figure 22. *Left:* Phase curves, integrated over 1.1–1.7 µm to simulate the HST-WFC3 instrument, of the four WASP-43b GCMs presented in the current study. The fluxes have been divided by the stellar flux integrated over the same range of wavelengths and multiplied by $(R_p/R_\star)^2$ in order to calculate the flux ratio received at Earth. Solid and dashed curves are of the full flux and reflected light only, respectively. 'I2S' is shorthand for 'improved two-stream', while 'ppm' stands for 'parts per million'. The light-blue curve is from Kataria et al. (2015); it represents their 1× solar metallicity, cloudy GCM simulation without TiO and VO. The cyan curve is from Mendonça et al. (2018a); a THOR simulation with dual-band grey radiative transfer with additional opacity on the night-side to mimic clouds. Black dots are the observed, band-integrated values from Stevenson et al. (2014); the dip at ∼180° is the secondary eclipse. The black line is their best fit to the phase curve with transit and secondary eclipse omitted (supplementary material in Stevenson et al. 2014). The data from Kataria et al. (2015) and Stevenson et al. (2014) were extracted from their plots using WebPlotDigitizer: https://apps.automeris.io/wpd. *Right:* Dayside (solid) and nightside (dashed) spectra compared to the stellar flux for all four models. Model spectra were output at $R = 500$ and degraded to $R = 50$ for plotting. For comparison we include the clear, solar composition model from Venot et al. (2020) in grey (see also Parmentier et al. 2016, 2021) and the grey radiative transfer case from Mendonça et al. (2018a), post-processed with 1D HELIOS. Also included are the observations from Stevenson et al. (2017) as black points and the re-processed *Spitzer* points from Mendonça et al. (2018a) as cyan points. The single data point from Fraine et al. (2021) for wavelengths 346–822 nm is an upper limit at 67 ppm.

DATA AVAILABILITY

The datasets were derived from sources in the public domain: https://github.com/exoclime.

REFERENCES

Abel M., Frommhold L., Li X., Hunt K. L. C., 2011, J. Phys. Chem. A, 115, 6805
Abel M., Frommhold L., Li X., Hunt K. L. C., 2012, J. Chem. Phys., 136, 044319
Adcroft A., Campin J.-M., Hill C., Marshall J., 2004, Mon. Weather Rev., 132, 2845
Agol E., Cowan N. B., Knutson H. A., Deming D., Steffen J. H., Henry G. W., Charbonneau D., 2010, ApJ, 721, 1861
Allard N. F., Spiegelman F., Kielkopf J. F., 2016, A&A, 589, A21
Allard N. F., Spiegelman F., Leininger T., Molliere P., 2019, A&A, 628, A120
Amundsen D. S., Baraffe I., Tremblin P., Manners J., Hayek W., Mayne N. J., Acreman D. M., 2014, A&A, 564, A59
Amundsen D. S. et al., 2016, A&A, 595, A36
Anderson J. L. et al., 2004, J. Clim., 17, 4641
Arcangeli J. et al., 2019, A&A, 625, A136
Azzam A. A. A., Tennyson J., Yurchenko S. N., Naumenko O. V., 2016, MNRAS, 460, 4063
Barber R. J., Strange J. K., Hill C., Polyansky O. L., Mellau G. C., Yurchenko S. N., Tennyson J., 2014, MNRAS, 437, 1828
Barman T. S., Hauschildt P. H., Allard F., 2001, ApJ, 556, 885
Barman T. S., Hauschildt P. H., Allard F., 2005, ApJ, 632, 1132
Barstow J. K., Heng K., 2020, Space Sci. Rev., 216, 82
Baudino J. L., Bézard B., Boccaletti A., Bonnefoy M., Lagrange A. M., Galicher R., 2015, A&A, 582, A83
Bell T. J., Cowan N. B., 2018, ApJ, 857, L20
Beltz H., Rauscher E., Brogi M., Kempton E. M. R., 2021, AJ, 161, 1
Burrows A. S., 2014a, PNAS, 111, 12601

Burrows A. S., 2014b, Nature, 513, 345

Burrows A., Sudarsky D., Hubbard W. B., 2003, ApJ, 594, 545

Burrows A., Hubeny I., Budaj J., Hubbard W. B., 2007a, ApJ, 661, 502

Burrows A., Hubeny I., Budaj J., Knutson H. A., Charbonneau D., 2007b, ApJ, 668, L171

Burrows A., Budaj J., Hubeny I., 2008a, ApJ, 678, 1436

Burrows A., Ibgui L., Hubeny I., 2008b, ApJ, 682, 1277

Burrows A., Rauscher E., Spiegel D. S., Menou K., 2010, ApJ, 719, 341

Carone L. et al., 2020, MNRAS, 496, 3582

Charnay B., Meadows V., Leconte J., 2015, ApJ, 813, 15

Cho J. Y. K., Polvani L. M., 1996, Science. 273, 335

Cho J. Y. K., Menou K., Hansen B. M. S., Seager S., 2003, ApJ, 587, L117

Cho J. Y. K., Menou K., Hansen B. M. S., Seager S., 2008, ApJ, 675, 817

Christie D. A. et al., 2021, MNRAS, 506, 4500

Chubb K. L., Tennyson J., Yurchenko S. N., 2020, MNRAS, 493, 1531

Cooper C. S., Showman A. P., 2005, ApJ, 629, L45

Cooper C. S., Showman A. P., 2006, ApJ, 649, 1048

Cowan N. B., Agol E., 2008, ApJ, 678, L129

Cox A. N., 2000, Allen's Astrophysical Quantities. Springer-Verlag, Berlin

De Wit J., Gillon M., Demory B. O., Seager S., 2012, A&A, 548, A128

Deitrick R., Mendonça J. M., Schroffenegger U., Grimm S. L., Tsai S.-M., Heng K., 2020, ApJS, 248, 30

Dobbs-Dixon I., Agol E., 2013, MNRAS, 435, 3159

Dobbs-Dixon I., Lin D. N. C., 2008, ApJ, 673, 513

Dobbs-Dixon I., Cumming A., Lin D. N. C., 2010, ApJ, 710, 1395

Dobbs-Dixon I., Agol E., Burrows A., 2012, ApJ, 751, 87

Drummond B. et al., 2018, ApJ, 855, L31

Drummond B. et al., 2020, A&A, 636, A68

Edwards J. M., Slingo A., 1996, Q. J. R. Meteorol. Soc., 122, 689

Flowers E., Brogi M., Rauscher E., Kempton E. M. R., Chiavassa A., 2019, AJ, 157, 209

Fortney J. J., Marley M. S., Lodders K., Saumon D., Freedman R., 2005, ApJ, 627, L69

Fortney J. J., Cooper C. S., Showman A. P., Marley M. S., Freedman R. S., 2006, ApJ, 652, 746

Fortney J. J., Lodders K., Marley M. S., Freedman R. S., 2008, ApJ, 678, 1419

Fortney J. J., Shabram M., Showman A. P., Lian Y., Freedman R. S., Marley M. S., Lewis N. K., 2010, ApJ, 709, 1396

Fraine J. et al., 2021, AJ, 161, 269

Freedman R. S., Marley M. S., Lodders K., 2008, ApJS, 174, 504

Frierson D. M. W., Held I. M., Zurita-Gotor P., 2006, J. Atmos. Sci., 63, 2548

Frierson D. M. W., Held I. M., Zurita-Gotor P., 2007, J. Atmos. Sci., 64, 1680

Fromang S., Leconte J., Heng K., 2016, A&A, 591, A144

Gandhi S., Jermyn A. S., 2020, MNRAS, 499, 4984

Ge H., Li C., Zhang X., Lee D., 2020, ApJ, 898, 130

Gillon M. et al., 2012, A&A, 542, A4

Goodman J., 2009, ApJ, 693, 1645

Grimm S. L., Heng K., 2015, ApJ, 808, 182

Grimm S. L. et al., 2021, ApJS, 253, 30

Guillot T., 2010, A&A, 520, A27

Guillot T., Showman A. P., 2002, A&A, 385, 156

Harris G. J., Tennyson J., Kaminsky B. M., Pavlenko Y. V., Jones H. R. A., 2006, MNRAS, 367, 400

Held I. M., 2005, Bull. Am. Meteorol. Soc., 86, 1609

Held I. M., Suarez M. J., 1994, Bull. Am. Meteorol. Soc., 75, 1825

Hellier C. et al., 2011, A&A, 535, L7

Heng K., 2012, ApJ, 761, L1

Heng K., 2017, Exoplanetary Atmospheres: Theoretical Concepts and Foundations. Princeton University Press, Princeton, New Jersey

Heng K., Kitzmann D., 2017, ApJS, 232, 20

Heng K., Showman A. P., 2015, Annu. Rev. Earth Planet. Sci, 43, 509

Heng K., Tsai S.-M., 2016, ApJ, 829, 104

Heng K., Menou K., Phillipps P. J., 2011a, MNRAS, 413, 2380

Heng K., Frierson D. M. W., Phillipps P. J., 2011b, MNRAS, 418, 2669

Heng K., Hayek W., Pont F., Sing D. K., 2012, MNRAS, 420, 20

Heng K., Mendonça J. M., Lee J.-M., 2014, ApJS, 215, 4

Heng K., Malik M., Kitzmann D., 2018, ApJS, 237, 29

Husser T. O., Wende-von Berg S., Dreizler S., Homeier D., Reiners A., Barman T., Hauschildt P. H., 2013, A&A, 553, A6

Jablonowski C., Williamson D. L., 2011, in Lauritzen P. H., Jablonowski C., Taylor M. A., Nair R. D., eds, Numerical Techniques for Global Atmospheric Models. Springer-Verlag, Berlin, p. 381

Kaspi Y., Flierl G. R., Showman A. P., 2009, Icarus, 202, 525

Kaspi Y., Showman A. P., Hubbard W. B., Aharonson O., Helled R., 2013, Nature, 497, 344

Kaspi Y. et al., 2018, Nature, 555, 223

Kataria T., Showman A. P., Lewis N. K., Fortney J. J., Marley M. S., Freedman R. S., 2013, ApJ, 767, 76

Kataria T., Showman A. P., Fortney J. J., Stevenson K. B., Line M. R., Kreidberg L., Bean J. L., Désert J.-M., 2015, ApJ, 801, 86

Keating D., Cowan N. B., 2017, ApJ, 849, L5

Kitzmann D., 2016, ApJ, 817, L18

Kitzmann D., Heng K., 2018, MNRAS, 475, 94

Kitzmann D., Patzer A. B. C., Rauer H., 2013, A&A, 557, A6

Komacek T. D., Showman A. P., 2016, ApJ, 821, 16

Komacek T. D., Tan X., 2018, Res. Notes Am. Astron. Soc., 2, 36

Komacek T. D., Showman A. P., Tan X., 2017, ApJ, 835, 198

Kreidberg L. et al., 2018, AJ, 156, 17

Langton J., Laughlin G., 2008, ApJ, 674, 1106

Lee E., Dobbs-Dixon I., Helling C., Bognar K., Woitke P., 2016, A&A, 594, A48

Lee E. K. H., Wood K., Dobbs-Dixon I., Rice A., Helling C., 2017, A&A, 601, A22

Lee E., Taylor J., Grimm S. L., Baudino J.-L., Garland R., Irwin P. G. J., Wood K., 2019, MNRAS, 487, 2082

Lee E. K. H., Casewell S. L., Chubb K. L., Hammond M., Tan X., Tsai S.-M., Pierrehumbert R. T., 2020, MNRAS, 496, 4674

Lewis N. K., Showman A. P., Fortney J. J., Marley M. S., Freedman R. S., Lodders K., 2010, ApJ, 720, 344

Li J., Goodman J., 2010, ApJ, 725, 1146

Li G., Gordon I. E., Rothman L. S., Tan Y., Hu S.-M., Kassi S., Campargue A., Medvedev E. S., 2015, ApJS, 216, 15

Lines S. et al., 2018, A&A, 615, A97

Lines S., Mayne N. J., Manners J., Boutle I. A., Drummond B., Mikal-Evans T., Kohary K., Sing D. K., 2019, MNRAS, 488, 1332

Liu B., Showman A. P., 2013, ApJ, 770, 42

Madhusudhan N., 2018, in Deeg H. J., Belmonte J. A., eds., Handbook of Exoplanets. Springer-Verlag, Berlin, p. 104

Majeau C., Agol E., Cowan N. B., 2012, ApJ, 747, L20

Malik M. et al., 2017, AJ, 153, 56

Malik M., Kitzmann D., Mendonça J. M., Grimm S. L., Marleau G.-D., Linder E. F., Tsai S.-M., Heng K., 2019, AJ, 157, 170

Manabe S., Smagorinsky J., Strickler R. F., 1965, Mon. Weather Rev., 93, 769

Mayne N. J., Baraffe I., Acreman D. M., Smith C., Wood N., Amundsen D. S., Thuburn J., Jackson D. R., 2014a, Geosci. Model Dev., 7, 3059

Mayne N. J. et al., 2014b, A&A, 561, A1

Mayne N. J. et al., 2017, A&A, 604, A79

Mayne N. J., Drummond B., Debras F., Jaupart E., Manners J., Boutle I. A., Baraffe I., Kohary K., 2019, ApJ, 871, 56

Meador W. E., Weaver W. R., 1980, J. Atmos. Sci., 37, 630

Mendonça J. M., 2020, MNRAS, 491, 1456

Mendonça J. M., Read P. L., Wilson C. F., Lee C., 2015, Planet. Space Sci., 105, 80

Mendonça J. M., Grimm S. L., Grosheintz L., Heng K., 2016, ApJ, 829, 115

Mendonça J. M., Malik M., Demory B.-O., Heng K., 2018a, AJ, 155, 150

Mendonça J. M., Tsai S.-m., Malik M., Grimm S. L., Heng K., 2018b, ApJ, 869, 107

Menou K., Rauscher E., 2009, ApJ, 700, 887

Menou K., Cho J. Y. K., Seager S., Hansen B. M. S., 2003, ApJ, 587, L113

Merlis T. M., Schneider T., 2010, J. Adv. Model. Earth Syst., 2, 13

Mihalas D., 1978, Stellar Atmospheres. W. H. Freeman, New York

Miller-Ricci E., Fortney J. J., 2010, ApJ, 716, L74

Mollière P., van Boekel R., Dullemond C., Henning T., Mordasini C., 2015, ApJ, 813, 47

Morris B. M., Heng K., Jones K., Piaulet C., Demory B.-O., Kitzmann D., Hoeijmakers H. J., 2021, preprint (arXiv:2110.11837)

O'Gorman P. A., Schneider T., 2008, J. Clim., 21, 5797

Oreshenko M., Heng K., Demory B.-O., 2016, MNRAS, 457, 3420

Parmentier V., Showman A. P., Lian Y., 2013, A&A, 558, A91

Parmentier V., Showman A. P., de Wit J., 2015, Exp. Astron., 40, 481

Parmentier V., Fortney J. J., Showman A. P., Morley C., Marley M. S., 2016, ApJ, 828, 22

Parmentier V. et al., 2018, A&A, 617, A110

Parmentier V., Showman A. P., Fortney J. J., 2021, MNRAS, 501, 78

Pauluis O., Czaja A., Korty R., 2008, Science, 321, 1075

Peixóto J. P., Oort A. H., 1984, Rev. Mod. Phys., 56, 365

Perna R., Heng K., Pont F., 2012, ApJ, 751, 59

Pierrehumbert R. T., 2010, Principles of Planetary Climate. Cambridge Univ. Press, Cambridge

Polyansky O. L., Kyuberis A. A., Zobov N. F., Tennyson J., Yurchenko S. N., Lodi L., 2018, MNRAS, 480, 2597

Pont F., Knutson H., Gilliland R. L., Moutou C., Charbonneau D., 2008, MNRAS, 385, 109

Pont F., Sing D. K., Gibson N. P., Aigrain S., Henry G., Husnoo N., 2013, MNRAS, 432, 2917

Rauscher E., Menou K., 2010, ApJ, 714, 1334

Rauscher E., Menou K., 2012, ApJ, 750, 96

Read P., 1986, Q. J. R. Meteorol. Soc., 112, 253

Roman M., Rauscher E., 2017, ApJ, 850, 17

Roman M., Rauscher E., 2019, ApJ, 872, 1

Roman M. T., Kempton E. M. R., Rauscher E., Harada C. K., Bean J. L., Stevenson K. B., 2021, ApJ, 908, 101

Rothman L. S. et al., 2010, J. Quant. Spec. Radiat. Transf., 111, 2139

Sainsbury-Martinez F. et al., 2019, A&A, 632, A114

Satoh M., 2002, Mon. Weather Rev., 130, 1227

Satoh M., 2003, Mon. Weather Rev., 131, 1033

Satoh M., Matsuno T., Tomita H., Miura H., Nasuno T., Iga S., 2008, J. Comput. Phys., 227, 3486

Schneider T., Liu J., 2009, J. Atmos. Sci., 66, 579

Schuster A., 1905, ApJ, 21, 258

Seager S., Sasselov D. D., 1998, ApJ, 502, L157

Seager S., Sasselov D. D., 2000, ApJ, 537, 916

Showman A. P., Guillot T., 2002, A&A, 385, 166

Showman A. P., Polvani L. M., 2010, Geophys. Res. Lett., 37, L18811

Showman A. P., Polvani L. M., 2011, ApJ, 738, 71

Showman A. P., Cooper C. S., Fortney J. J., Marley M. S., 2008, ApJ, 682, 559

Showman A. P., Fortney J. J., Lian Y., Marley M. S., Freedman R. S., Knutson H. A., Charbonneau D., 2009, ApJ, 699, 564

Showman A. P., Cho J. Y. K., Menou K., 2010, in Seager S., ed., Exoplanets. Univ. Arizona Press, Tucson, Arizona, p. 471

Showman A. P., Tan X., Parmentier V., 2020, Space Sci. Rev., 216, 139

Sing D. K., Désert J. M., Lecavelier Des Etangs A., Ballester G. E., Vidal-Madjar A., Parmentier V., Hebrard G., Henry G. W., 2009, A&A, 505, 891

Sing D. K. et al., 2016, Nature, 529, 59

Skinner J. W., Cho J. Y. K., 2021, MNRAS, 504, 5172

Sneep M., Ubachs W., 2005, J. Quant. Spectrosc. Radiat. Transfer, 92, 293

Sousa S. G. et al., 2018, A&A, 620, A58

Sousa-Silva C., Al-Refaie A. F., Tennyson J., Yurchenko S. N., 2015, MNRAS, 446, 2337

Spiegel D. S., Burrows A., 2010, ApJ, 722, 871

Staniforth A., Wood N., 2003, Mon. Weather Rev., 131, 1931

Steinrueck M. E., Parmentier V., Showman A. P., Lothringer J. D., Lupu R. E., 2019, ApJ, 880, 14

Stevenson K. B., 2016, ApJ, 817, L16

Stevenson K. B. et al., 2014, Science, 346, 838

Stevenson K. B. et al., 2017, AJ, 153, 68

Stock J. W., Kitzmann D., Patzer A. B. C., Sedlmayr E., 2018, MNRAS, 479, 865

Sudarsky D., Burrows A., Pinto P., 2000, ApJ, 538, 885

Sudarsky D., Burrows A., Hubeny I., 2003, ApJ, 588, 1121

Tan X., Komacek T. D., 2019, ApJ, 886, 26

Thalman R., Zarzana K. J., Tolbert M. A., Volkamer R., 2014, J. Quant. Spectrosc. Radiat. Transfer, 147, 171

Thrastarson H. T., Cho J. Y.-K., 2011, ApJ, 729, 117

Tinetti G., Liang M.-C., Vidal-Madjar A., Ehrenreich D., Lecavelier des Etangs A., Yung Y. L., 2007, ApJ, 654, L99

Tomita H., Satoh M., 2004, Fluid Dyn. Res., 34, 357

Toon O. B., McKay C. P., Ackerman T. P., Santhanam K., 1989, J. Geophys. Res., 94, 16287

Tremblin P. et al., 2017, ApJ, 841, 30

Tsai S.-M., Dobbs-Dixon I., Gu P.-G., 2014, ApJ, 793, 141

Tsai S.-M., Kitzmann D., Lyons J. R., Mendonça J., Grimm S. L., Heng K., 2018, ApJ, 862, 31

Vallis G. K., 2006, Atmospheric and Oceanic Fluid Dynamics. Cambridge Univ. Press, Cambridge

Vasavada A. R., Showman A. P., 2005, Rep. Prog. Phys., 68, 1935

Venot O. et al., 2020, ApJ, 890, 176

Virtanen P. et al., 2020, Nat. Methods, 17, 261

Wardenier J. P., Parmentier V., Lee E. K. H., Line M. R., Gharib-Nezhad E., 2021, MNRAS, 506, 1258

Washington W. M., Parkinson C., 2005, Introduction to Three-dimensional Climate Modeling. University Science Books, Sausalito, California

Yurchenko S. N., Tennyson J., 2014, MNRAS, 440, 1649

Yurchenko S. N., Barber R. J., Tennyson J., 2011, MNRAS, 413, 1828

Yurchenko S. N., Tennyson J., Barber R. J., Thiel W., 2013, J. Mol. Spectrosc., 291, 69

Zhang X., 2020, Res. Astron. Astrophys., 20, 099

APPENDIX A: REVIEW OF GOVERNING EQUATIONS OF ATMOSPHERIC DYNAMICS

The Navier–Stokes equation is a mathematical statement of the conservation of momentum for an atmosphere approximated as a fluid (e.g. Vallis 2006)

$$\frac{\partial \vec{v}}{\partial t} + \vec{v}.\nabla \vec{v} = \vec{g} - \frac{\nabla P}{\rho} - 2\vec{\Omega} \times \vec{v} + \nu \nabla^2 \vec{v} + \frac{\nu}{3} \nabla (\nabla.\vec{v}), \qquad (A1)$$

where $\vec{v}$ is the velocity, t is the time, $\vec{g}$ is the acceleration due to gravity, P is the pressure, ρ is the mass density, $\vec{\Omega}$ is the angular rotational frequency of the exoplanet, and ν is the molecular (kinematic) viscosity. The viscous terms (associated with ν; last two terms in preceding equation) are important only for small length-scales (i.e. small Reynolds numbers), typically well below the spatial resolution of the simulation grid, and may be neglected for large-scale circulation. Dropping these terms yields the Euler equations. Dobbs-Dixon & Agol (2013) retained these viscous terms presumably as a proxy for the turbulent viscosity, since turbulence may be approximated as a viscous process.

If one assumes a steady state for the radial component of equation (A1) and neglects the advective, Coriolis and viscous terms, then hydrostatic balance obtains

$$\frac{\partial P}{\partial r} = -\rho g. \qquad (A2)$$

Hydrostatic balance or equilibrium is *not* the approximation that the atmosphere is motionless in the radial/vertical direction. Rather, it is that the time-scale for the pressure gradient to balance gravity, which is $\sim H/c_s$ (where H is the pressure scale height and c_s is the sound speed), is the shortest time-scale of the system. Hydrostatic balance occurs essentially instantaneously. In other words, sound waves travel much faster than other waves (e.g. gravity, Rossby) in the system. In practice, if an explicit integration scheme is used for the radial momentum equation, then the time-step of integration is dominated by sound waves and the computational time becomes long (Dobbs-Dixon et al. 2012; Dobbs-Dixon & Agol 2013), because the

computational burden is dominated by having to *solve* for hydrostatic balance. Assuming hydrostatic balance makes the *choice* of filtering out *all* sound waves at the equation level. One may also implement an implicit integration scheme to selectively filter out sound waves; the HEVI scheme used in the `THOR` GCM is one such scheme (Satoh 2002, 2003; Tomita & Satoh 2004; Satoh et al. 2008; Mendonça et al. 2016; Deitrick et al. 2020).

The mass continuity equation is a mathematical statement of the conservation of mass for a fluid

$$\frac{\partial \rho}{\partial t} + \nabla . (\rho \vec{v}) = 0. \tag{A3}$$

When the approximation of hydrostatic balance is made, it is the mass continuity equation that provides the computation of the radial component of the velocity, since it is set to zero in the radial momentum equation in (A2).

The conservation of energy derives from the first law of thermodynamics for a fluid and is expressed as an evolution equation for the pressure, internal energy, kinetic energy, gravitational potential energy or total energy (e.g. chapter 9.4 of Heng 2017). It may also be expressed as an evolution equation for the potential temperature, which is the choice made in the `THOR` GCM (Mendonça et al. 2016; Deitrick et al. 2020). The heating term Q, which depends on the spatial gradient of the net flux, is present as one of the terms in the energy equation.

The primitive equations of meteorology are a reduced form of the mass continuity, Euler and energy equations, because three assumptions are made: hydrostatic balance, the shallow atmosphere approximation (where $1/r \approx 1/R$) and the so-called 'traditional approximation' (where the Coriolis and metric terms associated with the radial component of the velocity are neglected (e.g. Vallis 2006; section 9.6.2 of Heng 2017).

APPENDIX B: CORRESPONDENCE OF RADIATIVE TRANSFER EQUATIONS USED IN HENG ET AL. (2018) VERSUS MALIK ET AL. (2019)

Although Malik et al. (2019) implement the improved two-stream solutions of radiative transfer in the `HELIOS` code, equations (8)–(11) are listed for $E = 1$ (regular two-stream), where E is the ratio of first Eddington coefficients as defined by Heng et al. (2018). A fitting function for $E(\omega_0, g_0)$ is given in equation (31) of Heng et al. (2018). In this section, the equations with $E \neq 1$ (improved two-stream) are cast in the notation of Malik et al. (2019), because this corresponds to how they are written in the computer code. Unlike for Malik et al. (2019), the choice of $\epsilon = 1/2$ is made, but a value is not chosen for the second Eddington coefficient (ϵ_2). Following Malik et al. (2019), we define

$$\chi \equiv \zeta_-^2 \mathcal{T}^2 - \zeta_+^2,$$
$$\xi \equiv \zeta_+ \zeta_- \left(1 - \mathcal{T}^2\right),$$
$$\psi \equiv \left(\zeta_-^2 - \zeta_+^2\right) \mathcal{T}, \tag{B1}$$

where the coupling coefficients and transmission function are (Heng et al. 2018)

$$\zeta_\pm = \frac{1}{2} \left[1 \pm \sqrt{\frac{E - \omega_0}{E(1 - \omega_0 g_0)}}\right],$$
$$\mathcal{T} = e^{-2\sqrt{E(E - \omega_0)(1 - \omega_0 g_0)} \, \Delta\tau}, \tag{B2}$$

and the difference in optical depth between two points is given by $\Delta\tau$.

Consider an atmospheric layer with center index $i - 1$ and interfaces indexed by $i - 1$ (lower interface) and i (upper interface). For the outgoing (upward; $F_{\uparrow i}$) and incoming (downward; $F_{\downarrow i-1}$) fluxes, the boundary conditions are, respectively,

$$\frac{1}{\chi} \left(\psi F_{\uparrow i-1} - \xi F_{\downarrow i}\right),$$
$$\frac{1}{\chi} \left(\psi F_{\downarrow i} - \xi F_{\uparrow i-1}\right). \tag{B3}$$

The black-body terms are also straightforward to write down,

$$\frac{\Pi}{\chi} \left[B_i \left(\chi + \xi\right) - \psi B_{i-1} + \frac{B'}{2E(1 - \omega_0 g_0)} \left(\chi - \psi - \xi\right)\right],$$
$$\frac{\Pi}{\chi} \left[B_{i-1} \left(\chi + \xi\right) - \psi B_i + \frac{B'}{2E(1 - \omega_0 g_0)} \left(\xi + \psi - \chi\right)\right], \tag{B4}$$

where we have defined (Heng et al. 2018)

$$\Pi \equiv \pi \frac{1 - \omega_0}{E - \omega_0}. \tag{B5}$$

For the first equation of (B4), we note that Malik et al. (2019) erroneously wrote ψB_{i-1} as ξB_{i-1} in their equation (9). We verified that this is a typographical error that does not propagate into the `HELIOS` code.

For the terms associated with the direct stellar beam, several differences between the notation of Heng et al. (2018) and Malik et al. (2019) need to be reconciled. The beam impinges upon the atmosphere at an angle $\theta_\star$. Let $\mu_\star \equiv \cos\theta_\star$. Heng et al. (2018) define $\mu_\star$ as a positive quantity, whereas Malik et al. (2019) define it as a negative quantity. This difference in notation causes a flip in sign and implies that $C_\pm/F_\star$ (notation of Heng et al. 2018) corresponds to $\mathcal{G}_\mp$ (notation of Malik et al. 2019). Furthermore, what is written as $\mathcal{L}$ in equation (10) of Malik et al. (2019) is $C_\star/2F_\star$ in the notation of Heng et al. (2018). The stellar flux at the top of the atmosphere (TOA) is written as $F_{\star, \text{TOA}}$ in Malik et al. (2019) and $F_\star$ in Heng et al. (2018). Equation (6) of Malik et al. (2019) states the flux associated with the stellar beam

$$F_{\text{beam}, i} = -\mu_\star F_\star e^{\tau_i/\mu_\star}, \tag{B6}$$

which is a positive quantity as $\mu_\star < 0$. With this book-keeping of notation, the beam terms associated with $F_{\uparrow i}$ and $F_{\downarrow i-1}$, respectively, are

$$\frac{1}{\chi} \left[\psi \mathcal{G}_+ F_{\text{beam}, i-1} - (\xi \mathcal{G}_- + \chi \mathcal{G}_+) F_{\text{beam}, i}\right],$$
$$\frac{1}{\chi} \left[\psi \mathcal{G}_- F_{\text{beam}, i} - (\xi \mathcal{G}_+ + \chi \mathcal{G}_-) F_{\text{beam}, i-1}\right]. \tag{B7}$$

In a slight departure from equation (8) of Malik et al. (2019), we absorb the $1/\mu_\star$ coefficient associated with the beam terms into $\mathcal{G}_\pm$ itself,

$$\mathcal{G}_\pm = \frac{1}{2} \left\{\frac{\omega_0 \left[2E(1 - \omega_0 g_0) + \frac{g_0}{\epsilon_2}\right]}{4E\mu_\star^2 (E - \omega_0)(1 - \omega_0 g_0) - 1} \left[\mu_\star \pm \frac{1}{2E(1 - \omega_0 g_0)}\right] \right.$$
$$\left. \pm \frac{\omega_0 g_0}{2\epsilon_2 E(1 - \omega_0 g_0)}\right\}. \tag{B8}$$

Malik et al. (2019) assumed $\epsilon_2 = 1/2$, which does not correspond to the Eddington ($\epsilon_2 = 2/3$) or quadrature ($\epsilon_2 = 1/\sqrt{3}$) closures for the direct beam; ϵ_2 is undefined for the hemispheric closure (Meador & Weaver 1980; Toon et al. 1989). Physically, the choice of $\epsilon_2 = 1/2$ implies that an extra fraction $\mu_\star g_0$ of the stellar beam is scattered into the forward (downward) direction compared to the backward (upward)
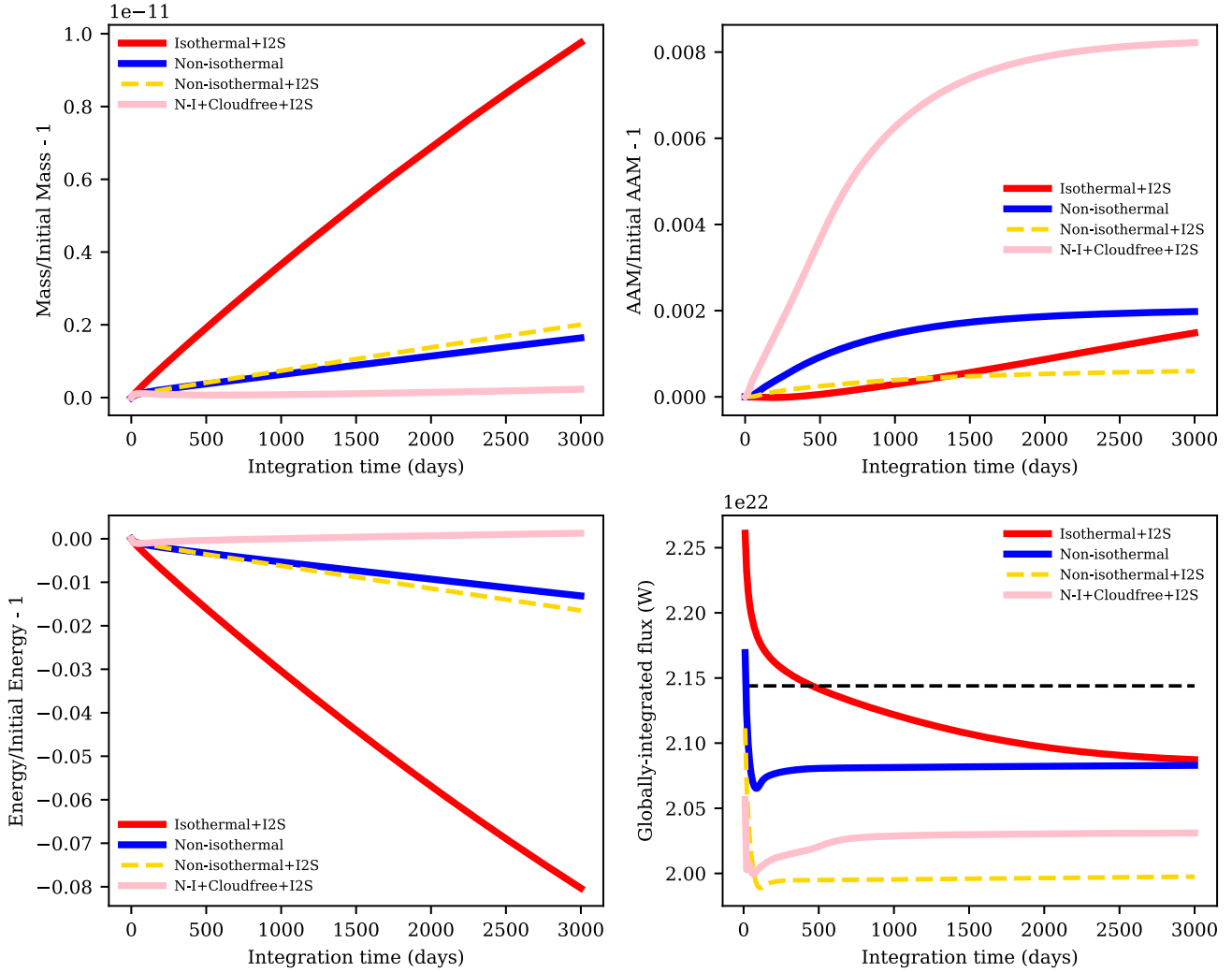
Figure B1. Evolution of the global mass (top left panel), axial angular momentum (AAM; top right panel), energy (bottom left panel) and globally integrated fluxes (bottom right panel) as a function of integration time. See text in Appendix D for description of expectations and precision of the conservation of each quantity. For the lower right panel, the black dashed curve is the incident stellar radiation at the top of the atmosphere; the other curves are the total outgoing fluxes (reflected starlight and thermal emission) at the top of the atmosphere for each model.

direction. In `THOR + HELIOS`, we allow ϵ_2 to be a user-specified choice; our chosen default is the Eddington closure ($\epsilon_2 = 2/3$).

APPENDIX C: RAYLEIGH SCATTERING CROSS-SECTIONS

For H_2-dominated atmospheres, the Rayleigh scattering cross-section is dominated by the contributions of molecular hydrogen and helium. It generally has the form (Sneep & Ubachs 2005),

$$\sigma_{\text{gas,scat}} = \frac{24\pi^3}{n_{\text{ref}}^2\lambda^4} \left(\frac{n_r^2 - 1}{n_r^2 + 2}\right)^2 K_\lambda, \tag{C1}$$

where λ is the wavelength, n_{ref} is a reference number density, K_λ is the King factor, and n_r is the real part of the index of refraction.

For molecular hydrogen, we have $K_\lambda = 1$, $n_{\text{ref}} = 2.686\,78 \times 10^{19}$ cm^{-3} and (Cox 2000),

$$n_r = 1.358 \times 10^{-4} \left[1 + 7.52 \times 10^{-3}\,\lambda'^{-2}\right] + 1, \tag{C2}$$

where $\lambda' \equiv \lambda/1\,\mu\text{m}$.

For helium (He), we have $K_\lambda = 1$, $n_{\text{ref}} = 2.546\,899 \times 10^{19}$ cm^{-3} and (Sneep & Ubachs 2005; Thalman et al. 2014)

$$n_r = 10^{-8} \left[2283 + \frac{1.8102 \times 10^{13}}{1.5342 \times 10^{10} - \lambda'^{-2}}\right] + 1. \tag{C3}$$

APPENDIX D: GLOBAL CONSERVATION OF QUANTITIES

Fig. B1 tracks the evolution of the global mass, angular momentum, energy and radiative fluxes for each of the 4 GCMs presented in the current study. The relative error in total mass of the atmosphere is small: less than 10^{-11} in all cases except the isothermal layers case, for which it is $\sim 2 \times 10^{-11}$. The poor convergence properties of the radiative transfer in this case apparently compounds upon the errors in the dynamical core. Axial angular momentum (AAM) is not as well conserved as a result of the use of linear momentum equations in the dynamical core (Mendonça et al. 2018b; Deitrick et al. 2020). However, the errors in AAM plateau as the flow reaches steady state, thus providing a useful convergence metric (Read

1986). All three non-isothermal layer simulations reach a steady-state of the flow in ~1000–2000 d. For the isothermal simulation, we again note the poor convergence, which in this case applies to the flow. The energy (lower left panel) is not necessarily conserved, because of the external forcing. Ideally, this will be conserved once radiative balance is achieved (lower right panel). All simulations except the isothermal layers case have converged, though there is a gap between in the incoming radiation and the end-state outgoing radiation – an error of ~ 3–7 per cent. This error is dominated by the numerical diffusion processes (hyper-diffusion and sponge layer). The numerical diffusion also causes the slow drift in the energy (lower left panel) in the non-isothermal cases.

APPENDIX E: COMPARISON TO MENDONÇA ET AL. (2018)

Fig. E1 shows the phase dependent spectra from our cloud-free GCM, compared to the simulations from Mendonça et al. (2018a) and Venot et al. (2020). The other simulations are removed for easier comparison. We have overplotted spectra from two additional tests. In the first, we have used the hemispherically averaged, line-of-sight corrected temperature-pressure profile from the day-side of the Mendonça et al. (2018a) GCM to produce spectra using our current $R = 500$ opacity table and 1D HELIOS. The result is quite similar to the spectrum produced by Mendonça et al. (2018a), which used a different opacity table, though with a similar list of sources. In the second, we used the day-side temperature–pressure profile from our cloud-free GCM, produced using the same averaging process, and the opacity table from Mendonça et al. (2018a) to produce another spectrum using 1D HELIOS. This result is now quite similar to our post-processed cloud-free GCM. Together, the two results show that the difference between the Mendonça et al. (2018a) spectrum and ours is not due to the minor differences in opacity tables (i.e. a few different molecules and different resolutions).

Inspecting the temperature–pressure profiles from our cloud-free GCM and the Mendonça et al. (2018a) GCM, we note that there is a difference of ~500 K in the photosphere (~0.01–0.1 bar) on the day-side. The increased long-wave emission in the Mendonça
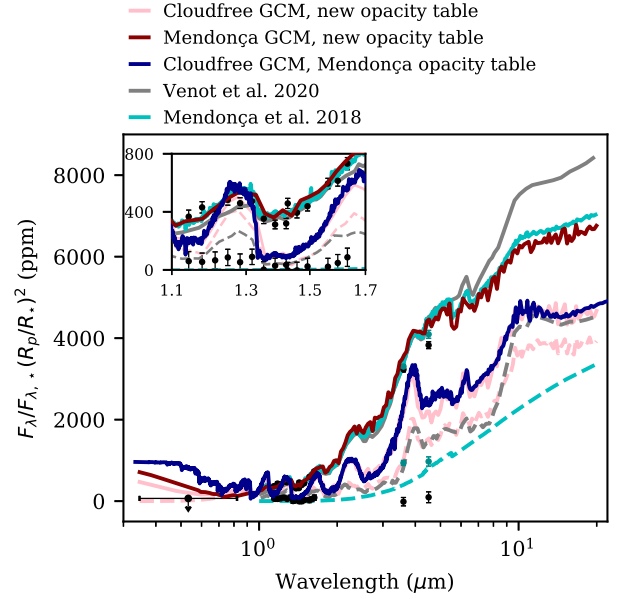

Figure E1. Phase dependent spectra from our cloud-free GCM and comparison GCMs (Mendonça et al. 2018a; Venot et al. 2020). Solid curves are the day-side emission and dashed are the night-side emission. These are identical to the data in Fig. 22. We have additionally plotted results from 1D HELIOS. The dark red curve utilized our current opacity table with temperature–pressure data from the day-side of the Mendonça et al. (2018a) GCM; the dark blue curve utilized the opacity table from Mendonça et al. (2018a) and temperature–pressure data from the day-side of our current cloud-free GCM.

et al. (2018a) GCM is thus a result of the higher temperatures in this region. For the moment it is unclear why the new model with k-tables is so much cooler than the dual-band grey RT model, but we have noticed that this difference tends hold in our testing for other planets.

This paper has been typeset from a TEX/LATEX file prepared by the author.